Surrogate model-based assessment of particle damage behaviour of Al-Zn-Mg alloy

Toda, Hiroyuki
Department of Mechanical Engineering, Kyushu University

Fukuda, Yuki
Department of Mechanical Engineering, Kyushu University

Li, Han
College of Informatics, Huazhong Agricultural University

Hirayama, Kyosuke
Department of Mechanical Engineering, Kyushu University

他

出版情報：Acta Materialia. 281, pp.120391-, 2024-12-01. Elsevier
バージョン：

Acta Materialia 281 (2024) 120391

Contents lists available at ScienceDirect

Acta Materialia

journal homepage: www.elsevier.com/locate/actamat

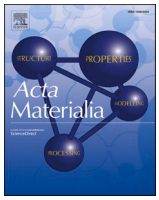

Surrogate model-based assessment of particle damage behaviour of Al—Zn—Mg alloy

Hiroyuki Toda [a,*], Yuki Fukuda [a], Han Li [b], Kyosuke Hirayama [a,c], Hiro Fujihara [a], Kazuyuki Shimizu [d], Yafei Wang [a], Jianwei Tang [a], Akihisa Takeuchi [e], Masayuki Uesugi [e]

[a] Department of Mechanical Engineering, Kyushu University, Motooka 744 Nishi-ku, Fukuoka 819-0395, Japan
[b] College of Informatics, Huazhong Agricultural University, 1, Shizishan Jie, Hongshan Qu, Wuhan 430070, China
[c] Department of Materials Science and Engineering, Kyoto University, Yoshida Honmachi, Sakyo-ku, Kyoto 606-8501, Japan
[d] Department of Physical Science and Materials Engineering, Iwate University, 3-18-8 Ueda, Morioka, Iwate 020-8550, Japan
[e] Japan Synchrotron Radiation Research Institute, 1-1-1, Kouto, Sayo-cho, Sayo-gun, Hyogo 679-5198, Japan

ARTICLE INFO

Keywords:
Surrogate modelling
Microtomography
Hydrogen embrittlement
Dispersion particles
Al-Zn-Mg alloys

ABSTRACT

Recent research has found some intermetallic compound particles with even stronger hydrogen trapping capacity (e.g., Al_7Cu_2Fe) than the age-hardening precipitates that are reported to be the origin of hydrogen embrittlement in aluminium. Such intermetallic compound particles can reduce hydrogen concentration at the interface between the precipitates and aluminium by absorbing hydrogen in their interiors, thus preventing the hydrogen embrittlement of aluminium. However, this cannot be achieved if the particles, which have absorbed large amounts of hydrogen, are damaged due to hydrogen embrittlement. In this study, the hydrogen embrittlement of aluminium was observed in situ by X-ray CT, and the damage behaviour was analysed of all the particles that were located in the gauge section of a single tensile specimen. After exhaustive quantification of the size, shape, and spatial distribution of the particles, coarsening processes identified highly correlated design variables. Subsequently, particle damage behaviour was analysed utilizing a surrogate model using a support vector machine. The damage to Al_7Cu_2Fe particles could be described only by design variables representing size and shape, while those representing spatial distribution were removed through the coarsening processes. No change was observed in the damage behaviour of Al_7Cu_2Fe particles with increasing hydrogen concentrations, and it was concluded that the dispersion of Al_7Cu_2Fe particles is effective in preventing hydrogen embrittlement of aluminium. The contribution of damaged particles to the formation of fracture surfaces and the damage behaviour of Mg_2Si particles, where damage is accelerated by hydrogen, were also analysed.

1. Introduction

In general, stress corrosion cracking occurs when all of the following three conditions are met: material, environment, and tensile load or tensile residual stress. However, stress corrosion cracking occurs in the common environment of moisture in the air rather than in specific acids, bases, or elements in aluminium alloys. In other words, with aluminium alloys, the conditions for stress corrosion cracking to occur are effectively reduced to two things: material and tensile load. In Al—Zn—Mg alloys, which are important in transportation applications, stress corrosion cracking is known to occur by a hydrogen embrittlement mechanism [1].

Various studies have been conducted on hydrogen embrittlement, both in terms of the mechanism and preventive measures. For example, HEDE (hydrogen enhanced decohesion), HELP, HESIV, HELP-mediated HEDE, and HELP+HEDE models are representative ones for the hydrogen embrittlement mechanisms [2–6]. In addition, various industrial methods and academic guiding principles have been provided for preventive measures, such as over-ageing [7–9], RRA (Retrogression and Re-aging) treatment [10–12], control of grain boundary morphology [13], control of intergranular and intragranular precipitates [13,14], control of intergranular electrochemical properties [15] and suppression of recrystallization [9,16–25].

In Al—Zn—Mg alloys, the interface most commonly associated with HEDE is grain boundaries, where hydrogen reduced cohesive energy, making them more susceptible to decohesion [2,3]. On the other hand,

* Corresponding author.
E-mail address: toda@mech.kyushu-u.ac.jp (H. Toda).

https://doi.org/10.1016/j.actamat.2024.120391
Received 7 March 2024; Received in revised form 23 August 2024; Accepted 9 September 2024
Available online 11 September 2024

HELP explains atomic-level mechanisms where hydrogen atoms interact with dislocations, influencing their motion and facilitating localized plastic deformation [4]. Other models called HELP mediated HEDE and HELP+HEDE models suggest a synergistic interaction between HELP and HEDE [3,6]. With regard to the HELP+HEDE model, it has been reported that simultaneous and concurrent effects of the different models are independently or mutually responsible for hydrogen embrittlement [6]. HESIV refers to a mechanism where the presence of hydrogen enhances the nucleation and clustering of vacancies under loading, acting as the sources for microvoid formation [5].

More recently, based on the hydrogen embrittlement mechanism revealed by Tsuru et al. of coherent interfaces between the η'/η precipitates and the aluminium matrix in Al—Zn—Mg alloys exhibiting spontaneous interface decohesion [26], several methods to prevent hydrogen embrittlement have been proposed. The basic idea is to add particles with higher hydrogen trapping energies than the coherent and semi-coherent interfaces between the precipitate and the aluminium matrix. This allows the majority of hydrogen in aluminium to be absorbed inside specific particles. This in turn reduces the amount of hydrogen at the precipitate-aluminium coherent and semi-coherent interfaces, thereby suppressing hydrogen embrittlement of aluminium alloys.

Particles that can prevent hydrogen embrittlement by such a mechanism include Al_7Cu_2Fe [27,28] and $Al_{11}Mn_3Zn_2$ [29] dispersed as relatively coarse intermetallic compound particles in the order of magnitude of microns in aluminium alloys, as well as $Al_2Mg_3Zn_3$ [30] dispersed as nanoscopic age-hardening precipitates (i.e., T phase). The interiors of these particles provide excellent hydrogen storage sites, combining high hydrogen trap energy with high trap site density for hydrogen. Indeed, our previous studies have experimentally confirmed the suppression of hydrogen embrittlement with increasing Fe content in practical Al—Zn—Mg alloys when the Fe content is varied significantly in the range of 1/10 to 10 times that of practical Al—Zn—Mg alloys [31]. The dispersion of Al_7Cu_2Fe particles has been shown to reduce the occupancy of hydrogen trap sites with hydrogen by two to three orders of magnitude at the semi-coherent interface between the η phase and the aluminium matrix [32]. However, there are a number of particles, such as Mg_2Si particles, in which their interiors have no capacity to trap hydrogen (i.e., a hydrogen trap energy of almost zero [33]).

Furthermore, when hydrogen is present inside pores as molecular hydrogen gas, premature growth and coalescence of the pores accelerates the ductile fracture of aluminium under external loading [34,35]. This is considered to be one form of hydrogen embrittlement in aluminium alloys, along with intergranular fractures, hydrogen-enhanced local plasticity, which promotes transgranular plastic deformation, and transgranular quasi-cleavage fractures [36]. But if a large amount of hydrogen is trapped inside intermetallic compound particles, such as Al_7Cu_2Fe, the intermetallic compound may be damaged at low stresses under the influence of hydrogen. Since Al_7Cu_2Fe particles do not exhibit plastic deformation, the hydrogen embrittlement mechanism of the particles is thought to be different from that of aluminium as described above. In this case, it is suggested that particle fracture could potentially be caused by a HEDE-like mechanism, either by debonding of the particle/aluminium interface or by decohesion of low cohesive energy crystallographic planes within the particle. The latter is more likely to occur when considering the hydrogen trapping energy of Al_7Cu_2Fe to be discussed in the discussion section. In any case, this will be confirmed experimentally in the present study. The voids formed by this may grow and coalesce prematurely, promoting ductile fractures in the same way as hydrogen pores. The same is true for ordinary ductile fracture, where voids created by particle fracture or interfacial debonding grow and coalesce. However, when hydrogen induces damage in intermetallic compound particles, the hydrogen is concentrated around the voids at the moment of void formation, so the hydrogen embrittlement mechanism of aluminium is triggered immediately after the damage occurs and damage development may be accelerated compared to the ordinary ductile fracture case.

If particle damage is enhanced by hydrogen absorption, it should be assumed to occur more significantly with smaller particles. Our preliminary experimental investigation found that small Al_7Cu_2Fe particles tended to be rather less damaged by external loading than larger particles [32]. On the basis of these results, we conclude that the damage to Al_7Cu_2Fe particles due to hydrogen absorption is unlikely to occur [32]. However, this conclusion was drawn from measurements of the size and sphericity of a total of 271 Al_7Cu_2Fe particles damaged by external loading, and it does not completely rule out the influence of hydrogen on particle damage, both in terms of data size and the accuracy of the particle characterisation analysis. In order to obtain more reliable conclusions, it would be useful to compare the damage behaviour of Al_7Cu_2Fe particles in samples with different hydrogen concentrations and statistically assess and understand under what geometrical conditions (particle size, shape, and spatial distribution) particle damage is likely to occur.

The authors recently proposed a method called Reverse 4D Materials Engineering (R4ME) [37], which enables a bird's eye view analysis of the statistical correlation between microstructures and macroscopic properties. It involves high-resolution 3D observation of the microstructure of a material and obtaining correlations between design variables representing the geometrical morphology of the microstructure and an objective function describing the macroscopic behaviour of the material. Due to the complexity of the microstructures of real-world materials and the limited spatial resolution of 3D imaging, a highly redundant quantitative evaluation that describes the microstructural morphology using a large number of design variables was first applied. Next, coarsening processes identified a limited number of design variables that were highly correlated with the objective function. A surrogate model was then constructed using the variables to represent the correlation between the selected important design variables and the objective function. A series of analyses were performed, based on high-resolution 3D images captured by high-resolution X-ray CT. These enabled the effects of complex microstructures, such as fine surface morphology and clustering of particles, to be assessed. R4ME has been used to assess the effects of dispersion particles and microscopic defects on the fracture behaviour of high-strength aluminium alloys. It can identify the dominant factors determining particle damageability, visualise the microstructure dependence of damage behaviour, and present the weakest and optimum microstructures [37–39].

In this study, the damage behaviour of more than 10,000 Al_7Cu_2Fe particles in the gauge section of a single tensile specimen was visualised in 4D under external loading using the X-ray microtomography technique. And the R4ME technique was applied to this data to identify the microstructural factors (particle properties) governing the damage behaviour of Al_7Cu_2Fe particles. In addition, the 4D trajectory prediction method in which fracture surfaces are time-traced back (a technique that precisely identifies the location of the fracture surfaces in 3D in a series of 3D images between the initial unloaded state and just before fracture) was applied to identify the particles that directly contributed to the fracture and to evaluate their geometric features. The same analysis was applied to Mg_2Si particles that do not absorb hydrogen. The objective was to assess the effectiveness of the technique in preventing hydrogen embrittlement of aluminium by storing hydrogen in particles with high hydrogen trap energy.

2. Experimental and analytical methods

2.1. 4D observation of hydrogen embrittlement in aluminium

After T651 tempering an A7075 alloy, micro-tensile specimens [40] for X-ray CT observation were prepared by electrical discharge machining (EDM) using water, which also served to hydrogen charge the specimens. The specimens were flat (0.6 mm thick) with a length and width of 0.7 mm and 0.6 mm, respectively, in the gauge section, and

they were arranged so that the thickness direction of the rolled plate was in the tensile direction. It has been reported that the hydrogen content of aluminium alloys increases by several tens of times due to the decomposition of water molecules by the flesh surface of an aluminium alloy during EDM using water [41]. In addition to the low-hydrogen (LH) material (3.1 mass ppm hydrogen content) to which EDM was applied, a high-hydrogen (HH) material was prepared by increasing the hydrogen content to 6.6 mass ppm by electric hydrogen charging. The hydrogen content of the specimens was measured by thermal desorption analysis. The heating rate was 1.5 °C/min, and the amount of hydrogen released up to 500 °C was measured.

In-situ observation of the tensile test was carried out using a projection-type X-ray CT at the beamline BL20XU of the synchrotron radiation facility SPring-8. The pixel size of the 3D images obtained was 0.50 μm^3, and the effective spatial resolution was 1.0 μ m. The X-ray energy was 20 keV, and the sample-to-detector distance was 20 mm. After loading at a strain rate of 2×10^{-3} with an average strain increment of about 0.8 %, the applied displacement was held for 10 min each time, including for the X-ray CT imaging. This load-hold cycle was repeated 24 and 17 times for the LH and HH materials, respectively.

The data obtained were reconstructed using the convolution back-projection method, and the reconstructed images were converted to 8-bit so that the grey scale range of the reconstructed images was 0–40 cm^{-1} in linear absorption coefficient.

2.2. 4D image analysis and statistical analysis

2.2.1. Identification of damaged particles that caused fractures

Using the 3D scattered discrete data interpolation method, the coordinates of the upper and lower fracture surfaces (point clouds) were trajectory-predicted from the post-fracture to the initial unloaded states by tracing backward in time, and the coordinates of the surfaces corresponding to the fracture surfaces were identified in the 3D images of the specimen captured before loading and during deformation. The 3D images of the specimen before loading and the predicted fracture surfaces were superimposed, and particles present in the vicinity of the fracture surfaces were identified as those that contributed to the formation of the fracture surfaces. For this purpose, the following image analyses were carried out.

(1) Extraction of fracture surface coordinates

As shown in Figs. 1(i) and 2(i), after binarising the upper and lower fractured specimens in the post-fracture 3D images, the fracture surface coordinates were measured pixel by pixel, and they were finally described in the form of point clouds representing the fracture surfaces (red [upper fracture surface] and yellow [lower fracture surface]) curves on the virtual cross sections in Figs. 1(i) and 2(i). The two point clouds corresponding to the upper and lower fracture surfaces (about 500,000 points each) were used for the fracture path estimation described in 2.2.1 (3). The 3D geometry of the fracture surface is shown as 3D images in Figs. 3(i) and 4(i).

(2) Particle trajectory tracking for fracture path estimation

First, all the Al_7Cu_2Fe and Mg_2Si particles were segmented, and 57,535 Al_7Cu_2Fe and 7485 Mg_2Si particles were identified in the gauge section of the HH specimen and 76,663 Al_7Cu_2Fe and 8991 Mg_2Si particles in the LH specimen. These particles could always be observed from the pre-loading to post-fracture states. Next, particle trajectory tracking was performed, which corresponds to identical particles sequentially between each successive 3D image to measure the physical displacement of each particle from the initial unloaded state to the post-fracture state. Identical particles were identified by considering the similarity of the coordinates, volumes, and surface areas of a couple of particles between each successive 3D image, and this was repeated sequentially from the post-fracture 3D image to the initial unloaded 3D image. Details of the particle trajectory tracking method are described elsewhere [41,42]

In addition, particles that were damaged during loading were identified. For this purpose, time-traced trajectory tracing of voids observed in the final loading step, which was just prior to fracture, was performed. The voids that could be traced back to the initial unloaded state were identified as pre-existing pores. These pores were precipitated molecular hydrogen during the thermo-mechanical treatments. As for the voids that could be traced to loading step n and not before loading step n, they were identified as voids that were initiated at loading step n [43]. For these voids, the particle that provided the initiation site for the void was identified by registering the 3D images captured at loading steps n and n-1 by affine transformation [43].

(3) Estimation of surfaces corresponding to the fracture paths in 3D images before and during deformation

After formulating the local displacement field using the trajectories of all the particles during specimen deformation, the coordinates of the upper and lower fracture surfaces (point clouds) were predicted backwards in time. Here, it was assumed that the positions corresponding to the upper and lower fracture surfaces would be displaced according to the formulated local displacement field during deformation of the specimen. In other words, it was assumed that there would be enough particles to predict with sufficient accuracy the physical displacements of the positions corresponding to the fracture surfaces. The validity of this assumption can be verified by evaluating the positional deviation between the trajectories of the upper and lower fracture surfaces, which were predicted separately.

The first step was to identify the particles present around the location of interest. For this purpose, a search range of radius r_0 was set, and r_0 was set so that at least five particles existed within the search range. In this study, r_0 was set to 44–76 μm.

Next, the interpolation coefficients c_j, which describe the local displacement field around a particle, were calculated for all the other particles present within the search range of the particle of interest, based on the particle displacement before and after deformation of the specimen.

$$u_i = \sum_{j=1}^{N} c_j \cdot g(\,\| p_i - p_j \|\,) \tag{1}$$

where u_i is the displacement of the i th particle before and after deformation, N is the number of particles in the search range, $g(r) = e^{-k \cdot r}$ is the radial basis function (RBFT), k is the coefficient of the RBFT, and $r = ||p_i - p_j||$ is the Euclidean distance before deformation between the i th particle and the other particles in the search range. The formulation of the local displacement field by all the particles is as follows:

$$\begin{pmatrix} u_{x1} & \cdots & u_{xN} \\ u_{y1} & \cdots & u_{yN} \\ u_{z1} & \cdots & u_{zN} \end{pmatrix} = \begin{pmatrix} c_{x1} & \cdots & c_{xN} \\ c_{x1} & \cdots & c_{yN} \\ c_{x1} & \cdots & c_{zN} \end{pmatrix} \begin{pmatrix} g(\|p_1 - p_1\|) & \cdots & g(\|p_1 - p_N\|) \\ \cdot & \cdot & \cdot \\ \cdot & \cdot & \cdot \\ g(\|p_1 - p_N\|) & \cdots & g(\|p_N - p_N\|) \end{pmatrix} \tag{2}$$

RBFT was used to improve the accuracy of trajectory predictions by ensuring that the effects of the displacements of the particles closer to the particle of interest in the search range rapidly increased. Once a set of interpolation coefficients c_j was obtained, trajectory predictions (calculation of the displacement, u, for each fracture surface coordinate) at any position could be performed according to the following formula:

$$u = \sum_{i=1}^{N} c_i \cdot g(\,\| P - p_i \|\,) \tag{3}$$

where P is the Euclidean distance between the fracture surface co-

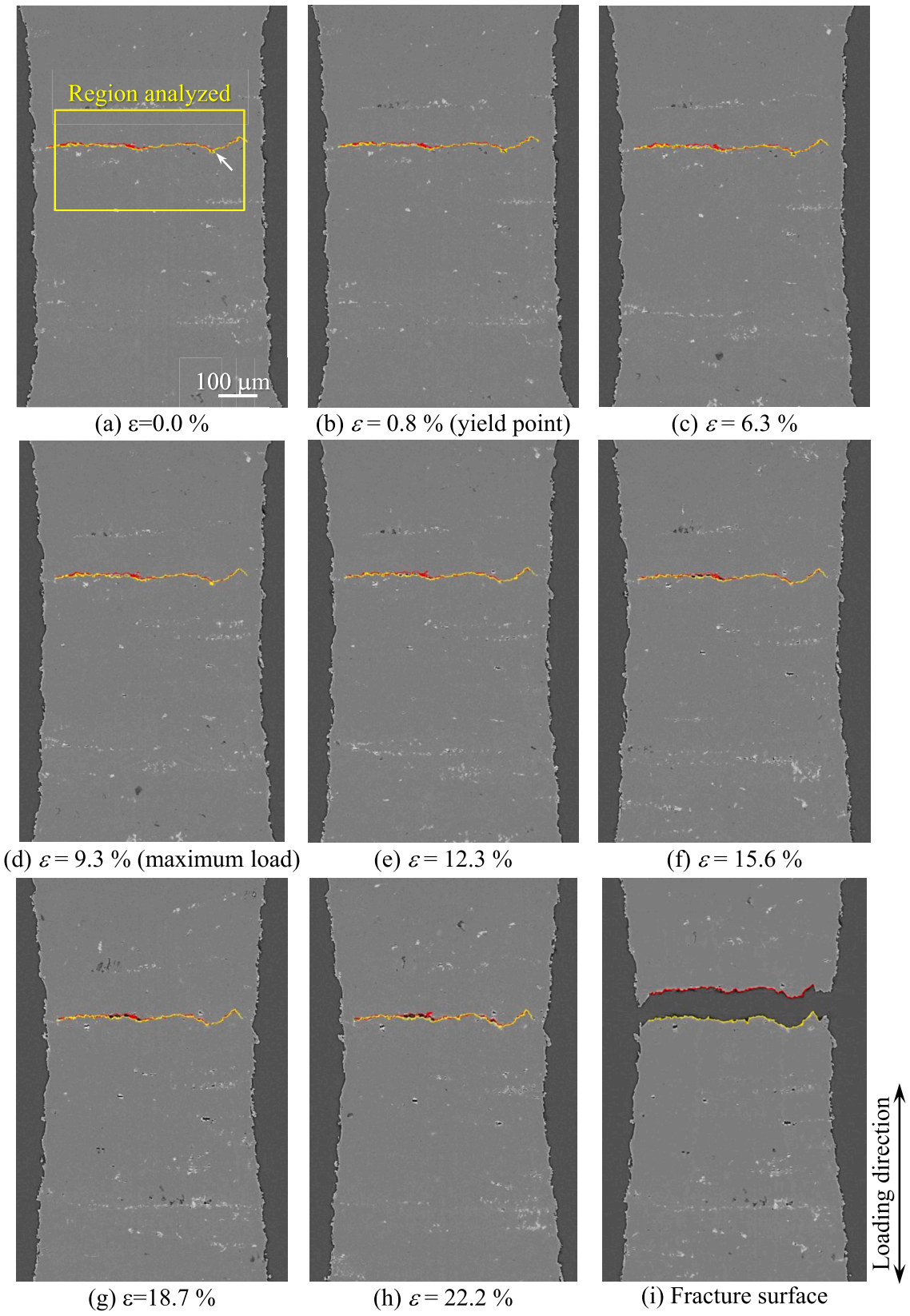

Fig. 1. Fracture path trajectories were estimated for the loading steps before fracture and superposed on an *x-z* tomographic virtual cross section in the LH material. The yellow and red lines are the fracture path trajectories for the lower and upper fracture surfaces, respectively.(For interpretation of the references to colour in this figure legend, the reader is referred to the web version of this article.)

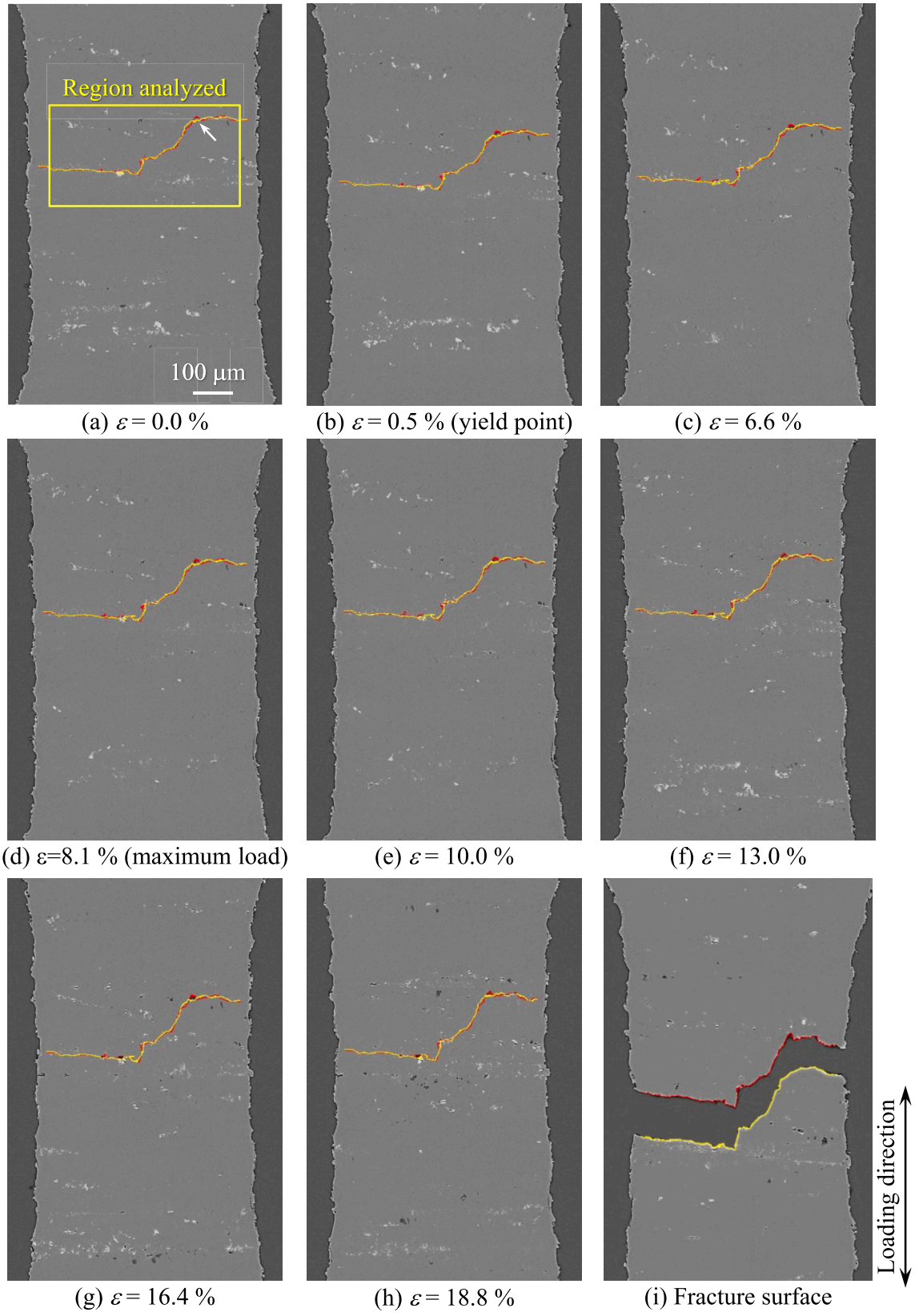

Fig. 2. Fracture path trajectories were estimated for the loading steps before fracture and superposed on an *x-z* tomographic virtual cross section in the HH material. The yellow and red lines are the fracture path trajectories for the lower and upper fracture surfaces, respectively.(For interpretation of the references to colour in this figure legend, the reader is referred to the web version of this article.)

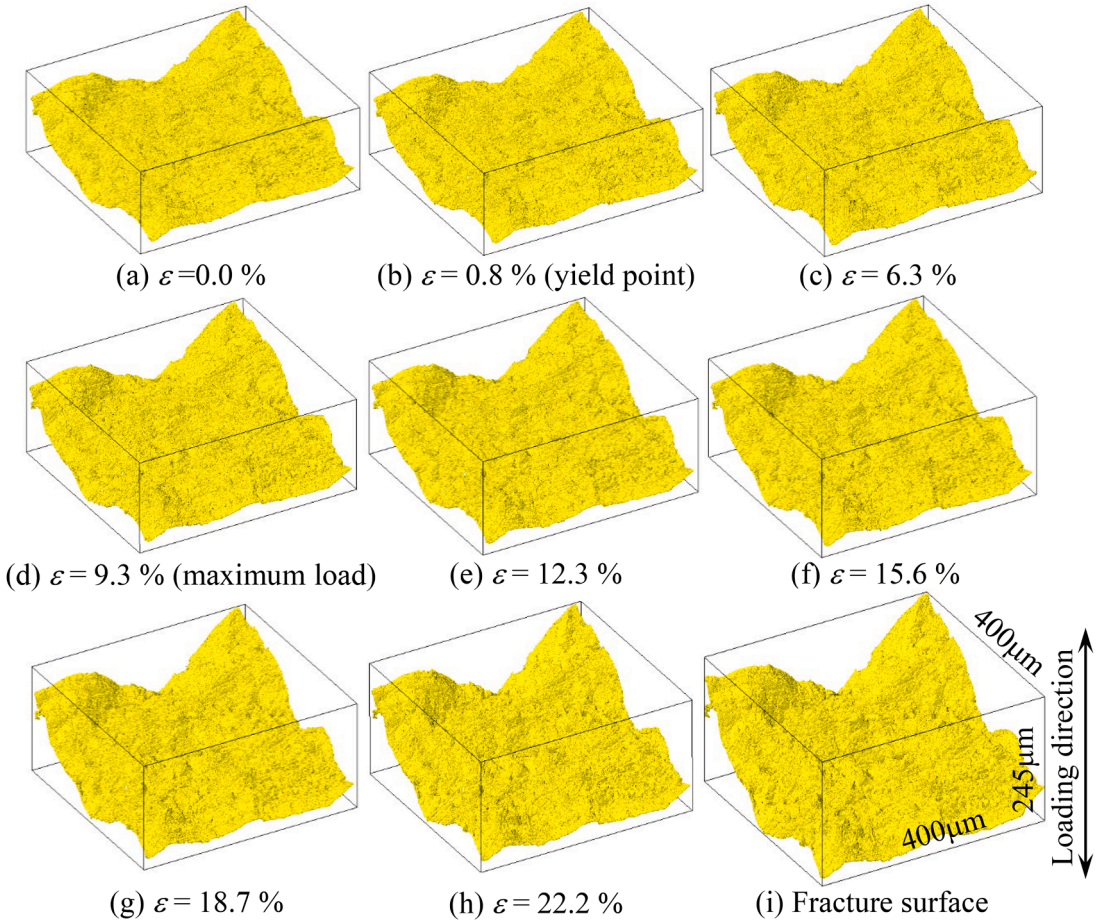

Fig. 3. 3D perspective views of the fracture path trajectories estimated for the loading steps before fracture in the LH material.

ordinates and each particle.

Using the estimated fracture path coordinates for the initial unloaded 3D images, damaged particles that directly contributed to ductile fractures were identified. The largest of the particle diameters along the three principal axes (the length of the major axis o^1 in Table 1) was calculated, and the particle with a distance between it and the predicted fracture surface coordinates of less than $\frac{o^1}{2}$ was identified as the particle that directly contributed to the ductile fracture.

It was also observed that the spatial distribution of particles differed at each loading step due to the effects of plastic deformation. The optimum values of r_0 and k were therefore different for each loading step. Therefore, r_0 was determined so that at least five or more particles were located within the search range, as described above. The spring model described below was used to calculate the optimum value of k:

$$\Delta E_{sp} = \frac{1}{N_{sp}} \sum_{i=1}^{N_{sp}} \frac{\left| b_{sp}^{i'} - b_{sp}^{i} \right|}{\left| b_{sp}^{i} \right|} \tag{4}$$

where ΔE_{sp} is the elastic energy of the spring, N_{sp} is the total number of virtual springs connecting each particle, and $b_{sp}^{i'}$, $b_{sp}^{i}$are the spring vector before and after deformation and the spring vector between the particle before deformation and the particle after deformation predicted by the RBFT function, respectively. Using Eq. (4), convergence calculations were performed to minimise ΔE_{sp}, and the optimum value of k was obtained for each loading step. Details of the fracture path estimation methods [35,42,43] and the spring model [43,44] are provided in the reference papers.

2.2.2. Surrogate model analysis of particle damage behaviour

The surrogate model optimisation method proposed in our previous publications [37,43] was applied. In order to quantitatively represent the microstructural properties, a number of design variables, such as size, shape, and orientation and an objective function that could quantitatively represent the analysis target were set. Next, coarsening processes were carried out to extract only design variables for which the interdependence between them was small and the correlation with the objective function was reasonably high. The coarsening processes mainly consisted of a first-stage principal component analysis to assess the interdependence between the design variables and a second-stage global sensitivity analysis to assess the correlation between the objective function and the design variables. A surrogate model was constructed using the extracted important design variables, and the relationship between microstructural properties and macro properties, etc. was evaluated. As the number of data points used in this study was relatively small for statistical analysis, a support vector machine with an infill sampling criteria was used to construct a surrogate model so that highly accurate analysis could be carried out with the limited data size. Due to space limitations, only the design variables and objective functions used are described below. The concept and details of the method are provided in a previous report [38].

(1) Design variables

Three categories of design variables were established for particle properties: particle size, shape, and spatial distribution. Possible design variables were evaluated and measured, as shown in Table 1. A total of 43 design variables were used to describe particle properties, 12, 24, and 7 for the three categories of size, shape, and spatial distribution, respectively. Particles exhibit

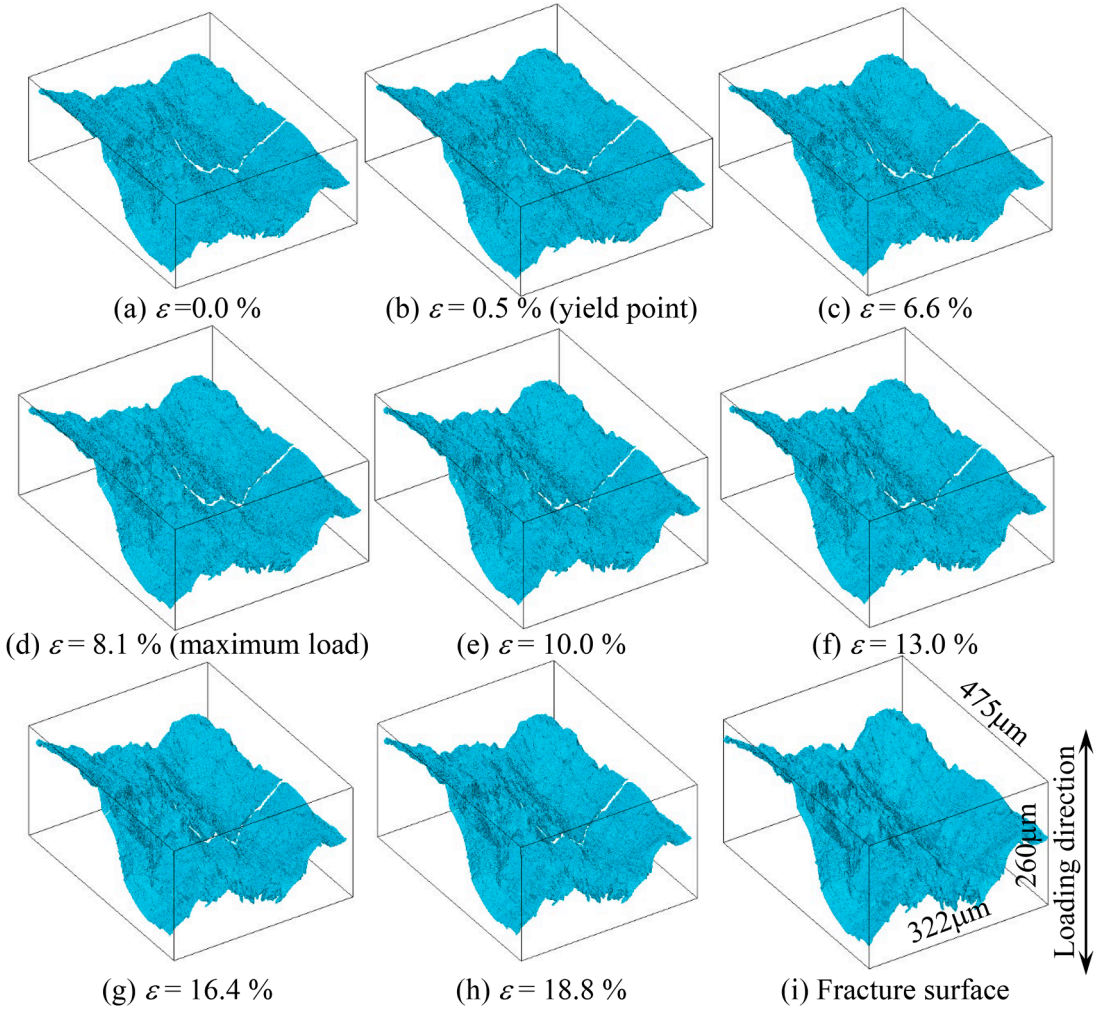

Fig. 4. 3D perspective views of the fracture path trajectories estimated for the loading steps before fracture in the HH material.

complex morphology, and shape needs to be quantified by various definitions, such as orientation, aspect ratio, deviation from cubic or spherical shape, connectivity, and surface complexity. In addition, direct size measurement is not always effective in X-ray CT because of the spatial resolution of the instrument, and the size of the microstructure is often relatively close. For example, if the thickness is close to the spatial resolution of the measurement system for an elliptical plate particle, attempts to compare particle size by measuring the particle volume will result in large errors. But if the height, width, and depth of the particle are measured by drawing a bounding box, which is the smallest cube containing the particle, an accurate assessment of size relationships may be possible [43]. From this perspective, the design variables representing the shape and spatial distribution pattern were highly redundant and used a large number of similar parameters, as shown in Table 1 [37,38].

(2) Objective functions

Two objective functions were defined for this study. The first (denoted as I_1) was the applied strain level at which the particles were damaged, and I_1 was normalised so that the macroscopic strain values between the initial unloaded state and just before fracture ranged from 0 to 0.5. The value for undamaged particles was set to 1. The second objective function was only for damaged particles, with 0 for particles that directly contributed to the formation of the fracture surface and 1 for particles that were damaged but did not contribute to the formation of the fracture surface (denoted as I_2).

3. Identification of damaged particles contributing directly to ductile fractures

3.1. Tensile test results

The stress-strain relationships of the tensile test obtained during in-situ observations are shown in Fig. S1. Due to the increase in hydrogen content caused by electric hydrogen charging, the fracture strain for the HH material was 15.1 % compared to 19.2 % for the LH material, which was about 21% lower. The X-ray CT observations were performed at an average strain interval of about 0.8%, so the number of X-ray CT observations, which caused stress drops of 8–27N in Fig. S1 due to stress relaxation, was 24 for the LH material and 17 for the HH material.

Fig. 1(a) and 2(a) show the particle distribution before loading for the LH and HH materials. The Al_7Cu_2Fe particles that appear white are mainly agglomerated near grain boundaries, and it appears that the coarse grain boundary particles formed during casting were crushed by cold rolling during the thermo-mechanical treatment. The dark grey Mg_2Si particles are present not only at grain boundaries but also within grains. When hydrogen concentrations are high in aluminium alloys, hydrogen precipitates as molecular gas in a wide size range from nanovoids [40] of a few nm in diameter to pores [34,35] of several μm in

Table 1
A list of the design variables for quantifying the size, shape, and spatial distribution of objects in aluminium alloys that were used in the application section of this paper [38].

Categories	Design variables	Remarks
I. Size (Sz) (12 parameters)	D, V, S	Equivalent diameter, volume and surface area, respectively
	B, L, W, T	Minimum volume bounding box; length of an object measured along the x direction; width of an object measured along the y direction; thickness of an object measured along the z direction
	p^1	Zeroth moment
	o^1, o^2, o^3	Length of the three principal axes
	$o = \frac{o^1 + o^2 + o^3}{3}$	Average length of the three principal axes.
	G	Geodesic distance
II. Shape (Sh) (24 parameters)	$o^4 = \frac{o^3}{o^1}, o^5 = \frac{o^2}{o^1}, o^6 = \frac{o^3}{o^2}$	Aspect ratio along the three principal axes
	θ	Angle between the loading direction and the first principal axis
	$f^1 = \frac{L}{W}, f^2 = \frac{L}{T}, f^3 = \frac{W}{T}$	Aspect ratio of a bounding box
	$f^4 = 6\sqrt{\pi}\frac{V}{\sqrt{S^3}}$, $f^5 = 48\pi^2\frac{V}{M^3}$, $f^6 = 4\pi\frac{S}{M^2}$	Deviation from spherical shape (M is the integral of mean curvature of an object)
	$f^7 = 216\frac{V^2}{S^3}$, $f^8 = 288\frac{V}{M^3}$, $f^9 = 16\frac{S}{M^2}$	Deviation from cubic shape
	$f^{10} = \frac{\pi G 3}{216V}$	Elongation index
	p^2, p^3, p^4	First moment invariants; p^2, p^3 and p^4 define the centre locations along the x, y and z directions respectively
	p^5, p^6, p^7	Second moment invariants, which represent the deviation from the centre (Measure of spread)
	p^8	Third moment invariant, which defines skewness (Measure of asymmetry)
	p^9	Fourth moment invariant, which defines kurtosis (Measure of tailedness)
	C	Mean curvature of an object
	E	Euler number, which describes the connectivity
III. Spatial distribution (D) (7 parameters)	K^2, K^3, K^5	Average distance within each k - nearest neighbour-hood (k = 2, 3, 5)
	l^2, l^3, l^5	Local volume fraction within K^2, K^3, K^5
	dm	Distance from a cluster centre

diameter. The relatively coarse ones grow and coalesce prematurely under external loading, promoting ductile fractures that reduce strength, ductility, etc. [34,35]. Figs. 1(a) and 2(a) show that such pores are rarely observed in the materials used.

3.2. Fracture path identification in 3D images before and during deformation

Figs. 1 and 2 show the changes in the identical virtual cross sections of the specimens during deformation and after fracture. The red and yellow lines shown in Fig. 1(i) and 2(i) are two point clouds (about 500,000 points each) representing the upper and lower fracture surface coordinates, respectively. The red and yellow lines shown in Figs. 1(a) to (h) and 2(a) to (h) are the estimated positions of the fracture paths calculated using the method described in Section 2.2.1. The yellow rectangles in Figs. 1(a) and 2(a) show the analysis region extended by 100 μm in both vertical and horizontal directions from the fracture surfaces. The size of this area is 490 × 42 × 245 μm for the LH material and 500 × 405 × 245 μm for the HH material. The fracture paths calculated from the upper and lower fracture surfaces deviated by up to 8 μm where coarse pores existed, as shown by the white arrows in Figs. 1 and 2. This means that the local deformation caused by the pores was less than the spatial resolution of the displacement field obtained from particle tracking. However, even in such cases, the pores were located near the middle of the two surfaces and did not interfere with the identification of the fracture origin. In other locations, the displacement of the two surfaces was less than 2 μm, indicating that the fracture path was estimated with sufficient accuracy.

In Figs. 1 and 2, fracture surface roughness is almost constant during uniform deformation, but it appears to gradually increase after the maximum load is passed. In fact, a comparison of the fracture surface roughness showed a 20 % increase between the initial unloaded state and just before fracture. This can be seen more clearly in the 3D images of the estimated fracture paths shown in Figs. 3 and 4. Such an increase in fracture surface roughness during deformation suggests that part of the fracture surface roughness was not due to the fracture path but to non-uniform deformation around the fracture path.

The number of particles located within the analysis area was 12,956 and 1474 for Al_7Cu_2Fe and Mg_2Si particles, respectively, in the LH material and 13,229 and 1511 for Al_7Cu_2Fe and Mg_2Si particles, respectively, in the HH material. Of these, 1414 Al_7Cu_2Fe and 190 Mg_2Si particles in the LH material and 1165 Al_7Cu_2Fe and 204 Mg_2Si particles in the HH material directly contributed to the formation of the fracture surfaces. Other particles that were damaged just before fracture but did not form a fracture in the analysis areas were 450 and 182 for Al_7Cu_2Fe and Mg_2Si particles, respectively, in the LH material and 321 and 178 for Al_7Cu_2Fe and Mg_2Si particles, respectively, in the HH material.

4. Characterisation of damaged particles

4.1. Selection of key design variables

Fig. 5 shows the results of the principal component analysis in the form of biplots. The arrows in the figures are the eigenvectors of each design variable, and the red dots are the particles. There were 861 total combinations of vectors, of which 37 for the Al_7Cu_2Fe particles and 37 for the Mg_2Si particles had angles of 5° or less. In this case, the interdependence between design variables was assumed to be strong, and vectors that were shorter (i.e., had fewer contributions) were removed. The first stage coarsening process reduced the number of design variables from 43 to 20 for Al_7Cu_2Fe particles and from 43 to 21 for Mg_2Si particles.

The design variables with Pearson correlation coefficients above 0.2 for the LH and HH materials were identical. Fig. 6 shows the design variables with Pearson correlation coefficients above 0.2, which were averaged over the LH and HH materials. This section shows the results of the global sensitivity analysis applied to the objective functions I_1 and I_2 by particle species. In the figures, design variables with high Pearson correlation coefficients are shown colour-coded by size, shape, and spatial distribution categories. It can be seen that for any of the objective functions and any of the particles, the design variables representing size and shape are highly correlated. Specifically, for the objective function I_1, the design variables representing particle size, elongation, surface shape, and shape complexity show a high correlation. On the other hand, the design variables representing spatial distribution were eliminated in the coarsening processes, with the exception of the two design variables. It is particularly interesting that no design variables representing spatial distribution remained for the Mg_2Si particles.

In order to provide surrogate models, the design variables with high Pearson correlation coefficients were selected, as shown in Fig. 6. The Pearson correlation coefficients for Mg_2Si particles were relatively high compared to the Al_7Cu_2Fe particles. Therefore, for Mg_2Si particles, the

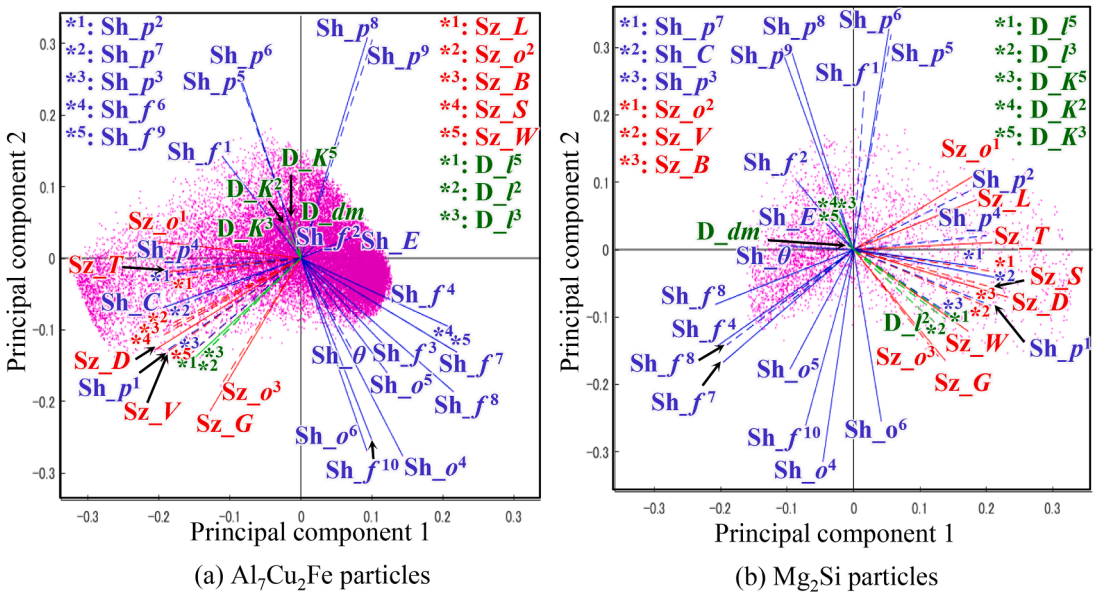

Fig. 5. Principal component score distributions are shown for the 43 design variables for Al_7Cu_2Fe and Mg_2Si particles that were obtained by applying the principal component analysis technique. Parameter symbols with "Sz", "Sh", and "D" represent design variables for size (shown in red), shape (blue) and spatial distribution (green), respectively. A total of 26,524 and 2985 particles were used for Al_7Cu_2Fe and Mg_2Si particles, respectively. The numbers of design variables were reduced to 20 and 21 for Al_7Cu_2Fe and Mg_2Si particles, respectively, by applying this coarsening process.(For interpretation of the references to colour in this figure legend, the reader is referred to the web version of this article.)

design variables with Pearson correlation coefficients greater than 80 % of the maximum Pearson correlation coefficient values of the design variables Sz_W and Sh_f^9 were adopted for both I_1 and I_2, and for Al_7Cu_2Fe particles, the criterion was eased to 75%. As a result, six and four design variables were selected for I_1 and I_2 for Al_7Cu_2Fe particles, respectively, and four and seven for Mg_2Si particles, respectively, which were then provided for surrogate modelling. In reference [37], a surrogate model was created using a similar approach, with four design variables selected, and its accuracy was verified by comparison with the results from the finite element analysis. The results show that most of the data points had a prediction error of less than 20%. Therefore, of the number of design variables selected in this study, between four and seven can be considered reasonable.

4.2. Surrogate model analysis results

4.2.1. Particle damage susceptibility (objective function I_1)

(1) Al_7Cu_2Fe particles

The surrogate model analysed the damage to Al_7Cu_2Fe particles with respect to the objective function I_1. In order to facilitate its visual evaluation, 3D response surfaces showing the relationships between I_1 and Sz_D and Sh_C, which were the design variables with the highest Pearson correlation coefficients, are shown in Fig. 7(a). The response surfaces show both the 3D shapes and colour contours of particle damage susceptibility in the range from blue (high I_1) to red (low I_1). In this case, the remaining four design variables (Sz_G, Sz_o, Sz_T and Sh_f^4) were set to their optimum values (Sz_G = 12.7 μm, Sz_o = 1.9 μm, Sz_T = 4.5 μm, Sh_f^4 = 0.59). The same applies to other response surfaces after this. Particle damage tended to occur when both Sz_D and Sh_C were higher than 0.8 for Al_7Cu_2Fe particles in both LH and HH materials. Here, Sh_C was the mean curvature of particle surfaces, and Sz_D was the sphere equivalent diameter of particles. It implies that particles that present coarse and complex shapes are more susceptible to damage. In general, it is known that coarse particles in materials have a lower in-situ strength and are more prone to damage.

Notably, there was little difference between the LH and HH materials in terms of both the minimum values and the shape of the response surfaces. If hydrogen causes particle damage, it is likely that a hydrogen concentration gradient is generated in the particles depending on the hydrogen diffusion time, and that this effect differs for different particle sizes. In this case, the average hydrogen concentration would be expected to increase for smaller particles, leading to an increased tendency towards hydrogen embrittlement. However, no such tendency is seen in Fig. 7(a), so it can be concluded that the Al_7Cu_2Fe particles had no tendency toward hydrogen embrittlement. However, with (Sz_D, Sh_C) = (1, 1) as the centre (i.e., the minimum value of I_1), it can be seen that the HH material was prone to damage in a slightly narrower range (i.e., particles that were coarser and with distorted shapes). In other words, the HH material tended to be less prone to damage than the LH material for moderate Sz_D and Sh_C values. In general, at high hydrogen concentrations, aluminium deformation was localised [40,41], and plastic strain increased rapidly within a limited band. In contrast, the plastic strain decreased in many other regions. Plastic deformation of aluminium leads to an increase in the internal stress of particles, which promotes particle fractures [45]. Therefore, it can be inferred that the strain localisation of aluminium by hydrogen usually works in the direction of inhibiting the occurrence of damage in particles with moderate Sz_D and Sh_C values, which are relatively close to the damage initiation conditions. This may have led to the subtle differences between the LH and HH materials in the response surfaces in Fig. 7(a).

In the introduction, the results of a preliminary experimental investigation were introduced in which the behaviour of several hundred particles was semi-quantitatively investigated on the basis of geometric measurements of size and sphericity. It was found that there was a tendency for small Al_7Cu_2Fe particles to be less damaged by external loading even at high hydrogen concentrations [32]. The results in Figs. 6 and 7 show a dramatically improved statistical certainty of this finding and allow identification of the dominant geometric design variable. With the Al_7Cu_2Fe particles, there was a strong tendency for coarse and

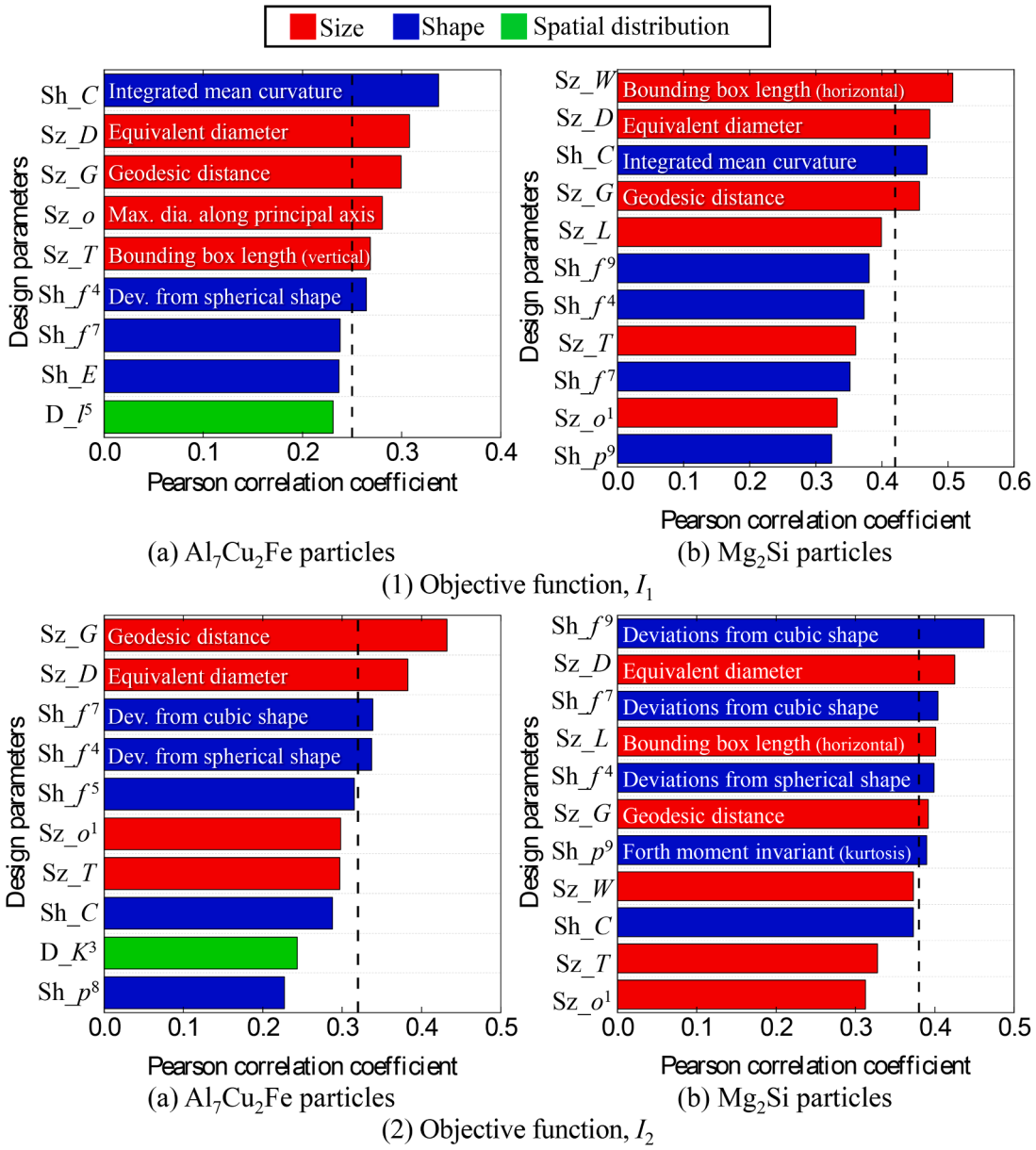

Fig. 6. The results of the global sensitivity analysis are shown, which represent the Pearson correlation coefficients for the objective functions (1) I_1 and (2) I_2 for (a) Al_7Cu_2Fe particles and (b) Mg_2Si particles. Bars highlighted in red, blue, and green are design variables for size, shape, and spatial distribution, respectively.(For interpretation of the references to colour in this figure legend, the reader is referred to the web version of this article.)

distorted particles to be damaged, and this tendency was somewhat facilitated by increasing hydrogen concentrations. In addition, particle size, shape discontinuities, elongation, and orientation in the loading direction, which lead to stress concentration and increased stress triaxiality, can be said to be important factors governing particle damage.

Fig. 8(a) shows, for reference, actual particles extracted from the image data with Sz_*D* and Sh_*C* values closest to the weakest Al_7Cu_2Fe particle predicted by the surrogate model (particles with the lowest I_1) and the strongest Al_7Cu_2Fe particle (particles with the highest I_1) and, therefore, which particles should be removed to maintain the mechanical properties of aluminium alloys. The strongest particles were small particles with simple shapes, that is, relatively close to a sphere. The weakest particles were coarse particles with complex shapes, and it appears that many coarse particles were connected.

The data and response surfaces are then projected onto the Sh_*C* - Sz_*D* 2D planes in Fig. 9(1)(a) to compare the 3D response surface of the HH material in Fig. 7(a)(2) with the experimental data. The data for all the particles are shown as black (undamaged) and white (damaged) dots. The two yellow dots are the predicted positions of the strongest and weakest particles. The range of 0.2 after normalisation was defined for Sh_*C* and Sz_*D* (yellow dotted squares in both the figures), and the damage ratio, r_D, of the particles was calculated within this range. It can be seen that the damage ratio near the weakest particle (r_D = 20.5 %) is more than 50 times higher than for the strongest particle (r_D = 0.4 %). This implies that the accuracy of the response surfaces was sufficiently high.

(2) Mg_2Si particles.

Fig. 7(b) shows the results of the damage analysis for Mg_2Si particles with respect to the objective function I_1. The design variables Sz_*D* and Sz_*G* were used, with Sz_*G* representing the shortest geodesic length of a particle, meaning it encompassed

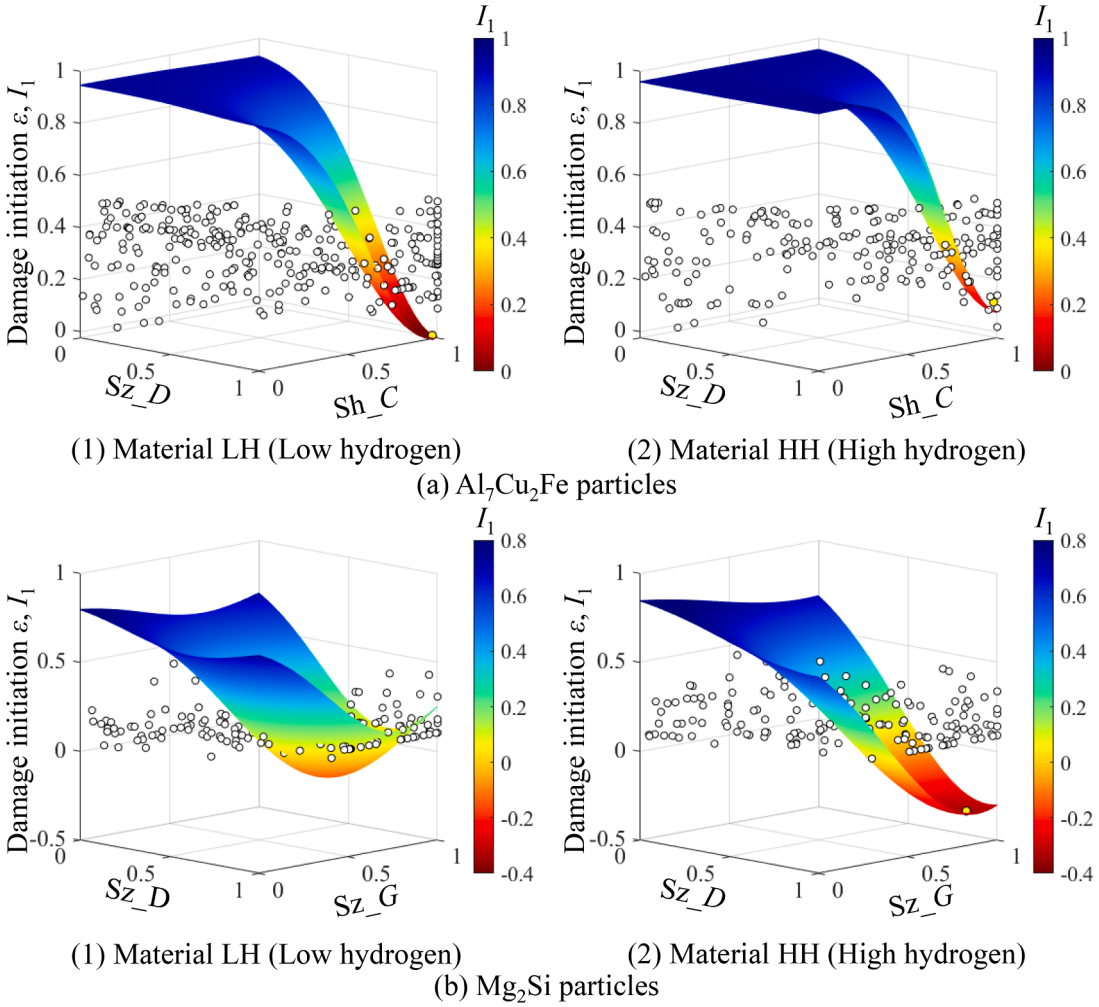

Fig. 7. 3D contour maps of the objective function I_1 predicted by the surrogate model are shown. The effects of hydrogen concentrations ((1) low and (2) high) are shown for (a) Al_7Cu_2Fe and (b) Mg_2Si particles. Two design variables were selected to show a 3D design space for each graph, with the remaining design variables fixed at their optimum values. The experimental results are shown as white dots.

both size and shape. Fig. 9(1)(b) compares the response surfaces and experimental data in the HH material. It can be seen that the damage ratio is about 11 times higher than that of the strongest particles. Therefore, it can be said that even for Mg_2Si particles, the trends of the surrogate model response surfaces and the experimental data were in good statistical agreement.

The weakest particle predicted for the LH material was 4.7 μm for Sz_*D*, 6.1 μm for the HH material, and 17.8 μm and 21.8 μm for Sz_*G*, respectively, with the positions of the weakest particle slightly different between the LH and HH materials. However, the strongest particles were 1.9 μm for both the LH and HH materials in Sz_*D* and were almost equal at 4.3 μm and 4.4 μm for Sz_*G*, respectively. Judging from the shape of the response surfaces, the tendency to fracture was higher for Mg_2Si particles with larger and more distorted shapes, irrespective of the hydrogen concentration. After normalisation, the response surface shapes of the LH and HH materials were almost identical up to the values of 0–0.6 to 0.7 for Sz_*D* and Sz_*G*. For the LH material, I_1 increased when Sz_*D* and Sz_*G* exceeded that level. But for the HH material, there was a clear difference with further decreases. Presumably this is because with a finite diffusion time, the average hydrogen concentration of the coarse particles in the LH material was reduced and damage suppressed. But with the HH material, the average hydrogen level reached a level sufficient for particle damage to occur.

From the above, it appears that particle damage was promoted by hydrogen in Mg_2Si particles. In a previous report referenced in the introduction, it was observed that high hydrogen concentrations promoted interfacial decohesion between particles and the aluminium matrix, albeit semi-quantitatively [32]. However, the effect of particle properties was not clear. Fig. 8(b) shows actual particles extracted from experimental data with Sz_*D* and Sz_*G* values closest to the weakest and strongest Mg_2Si particles predicted by the surrogate model. The strongest particles have extremely small flat surfaces that are prone to interfacial delamination. In addition to the effect of particle size, it can be seen that the damage tendency is stronger for particles with horizontally oriented, easily debonded interfaces.

4.2.2. Ease of forming fracture surfaces from damaged particles (objective function I_2)

The objective function I_2 was only for damaged particles and it took smaller values for particles that directly contributed to the formation of fracture surfaces. The 3D response surfaces showing the relationships between design variables Sz_*G* and Sz_*D* with high Pearson correlation coefficients and I_2 for Al_7Cu_2Fe particles are shown in Fig. 10(a), which uses the surrogate model constructed with the design variables selected in Fig. 6 and the objective function I_2.

The Sz_*D* values of the damaged particles with the highest tendency to form fracture surfaces in the HH and LH materials were 4.4 μm and

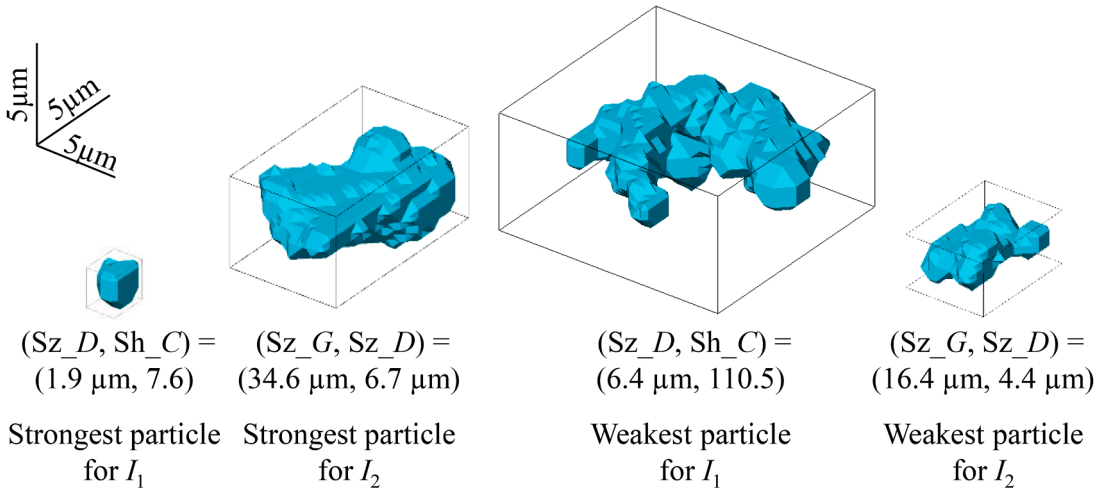

(a) Al_7Cu_2Fe particles (Average values: (Sz_*D*, Sh_*C*, Sz_*G*) = (3.3 μm, 36.1, 16.0 μm))

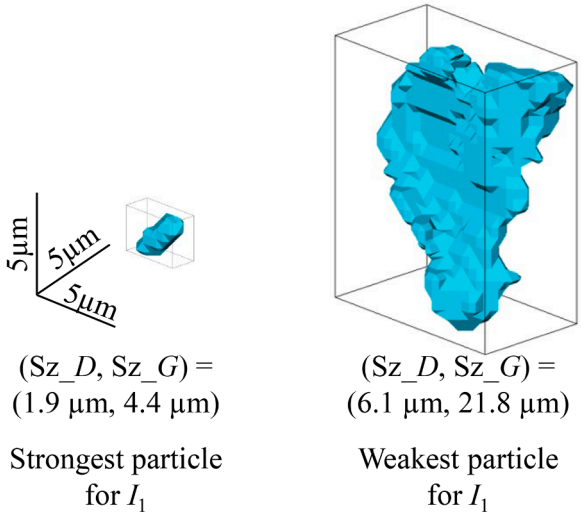

(b) Mg_2Si particles (Average values: (Sz_*D*, Sz_*G*) = (4.1 μm, 13.5))

Fig. 8. Examples of the weakest and strongest particles for the objective functions I_1 and I_2 for Al_7Cu_2Fe and Mg_2Si particles, which have been selected from the original 3D image according to the predicted optimum and worst values of the design variables. The values of (Sz_*D*) and (Sh_*C*) and (Sz_*D*) and (Sz_*G*) for the selected particles are shown for Al_7Cu_2Fe and Mg_2Si particles, respectively, together with the average values.

3.8 μm, respectively. Those with the lowest tendency had Sz_*D* values of 6.7 μm and 6.5 μm for materials HH and LH, respectively. The Sz_*G* values of the damaged particles with the highest tendency to form fracture surfaces in the HH and LH materials were 16.4 μm and 15.5 μm, respectively. Those with the lowest tendency had Sz_*G* values of 34.6 μm and 33.0 μm, respectively. Regardless of the high or low propensity to form fracture surfaces, there is no significant difference between the HH and LH materials in terms of both the design variable values of the particles, as was so in objective function I_1. Therefore, it can be seen that the effect of hydrogen on the tendency to form fracture surfaces from damaged Al_7Cu_2Fe particles was also small, as was the tendency for particle damage. However, the range of fracture surface forming particles on the Sz_*D* - Sz_*G* plane was extended in the HH material, as shown in Fig. 9 (The region size of $I_2 > 0.2$ was 0.75 for the LH material and 0.52 for the HH material). In particular, such broadening is more obvious in the Sz_*D* - axis direction than in the Sz_*G* - axis direction. This can be explained by the deformation localisation of aluminium at high hydrogen concentrations, which is described in 4.2.1(1). In other words, under high concentrations of hydrogen, the plastic strain increased rapidly in some regions, which led to macroscopic fractures. Therefore, under high concentrations of hydrogen, the fracture surface formation process, which links particle clusters, as seen in the LH material, was overshadowed, and fracture surfaces were formed by linking damaged particles within the strain-localised region. Therefore, it is believed that a wider range of shapes and sizes of damaged particles form fracture surfaces.

In Fig. 9(2)(a), the 3D response surface of the HH material is projected onto the Sz_*G* - Sz_*D* 2D plane, and the data for all the damaged particles are plotted as black dots (there is no contribution to fracture surface formation) and white dots (there is a contribution to fracture surface formation). The two yellow dots are the predicted results of the damaged particles with the highest and lowest tendencies to form fracture surfaces. A range of 0.2 was defined around these points for Sz_*G* and Sz_*D*, respectively (the yellow dotted squares), and the fracture surface formation ratio, r_F, was calculated within this range. The r_F values for the damaged particles with the highest and lowest propensity to form fracture surfaces differed by a factor of only 2.41. This is in contrast to the damage propensity, which differed by a factor of more than 50 for the r_D values. In other words, the extent that the fracture surface formation tendency of damaged particles depended on the design variables was relatively moderate compared to the objective function I_1.

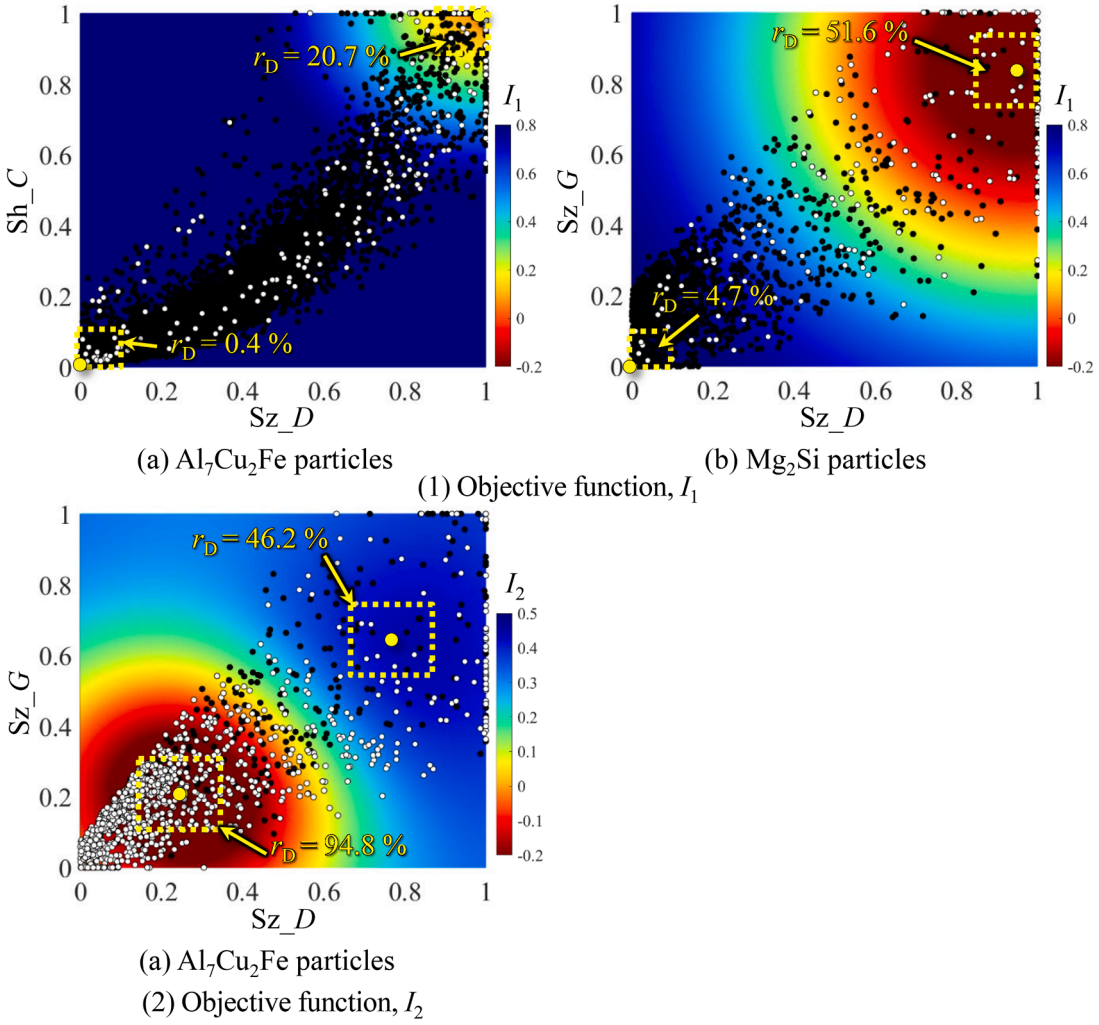

Fig. 9. Contour maps of the objective functions (1) I_1 and (2) I_2 predicted by the surrogate model are shown. The 3D contour maps in Figs. 7 and 10 were projected onto the 2D design space to enhance visibility for (a) Al_7Cu_2Fe and (b) Mg_2Si particles in the HH material. The selected design variables that are not shown here were fixed at their optimum values. Fractured and intact particles in the experiments are shown as white and black dots, respectively.

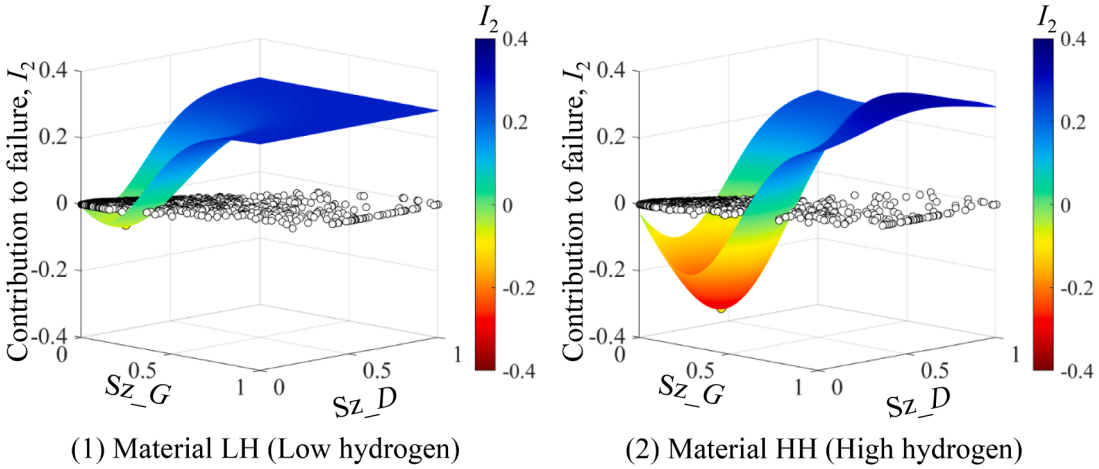

Fig. 10. 3D contour maps of the objective function I_2 predicted by the surrogate model are shown. The effects of hydrogen concentrations ((1) low and (2) high) are shown for Al_7Cu_2Fe particles. Two design variables were selected to show a 3D design space for each graph, with the remaining design variables fixed at their optimum values. The experimental results are shown as white dots.

Fig. 8(a) shows the actual damaged Al_7Cu_2Fe particles in the experimental data with Sz_*G* and Sz_*D* values closest to the damaged Al_7Cu_2Fe particles with the strongest tendency to form fracture surfaces (particle properties giving the lowest I_2 value) predicted by the surrogate model and those with the weakest tendency (particle properties giving the highest I_2 value). Although the difference in shape is not very strong, it can be seen that the tendency to form fracture surfaces is weaker for coarse damaged particles. This may be because coarse particles tend to exist independently, whereas particle clusters are composed of relatively small particles.

5. Discussions relating to the guiding principles for the prevention of hydrogen embrittlement

5.1. Hydrogen embrittlement of particles and aluminium

The size of the Al_7Cu_2Fe and Mg_2Si particles dispersed in the materials used is in the order of magnitude of microns, and it is assumed they have rather coarse microstructural features for practical structural metallic materials. It is well known that coarse particles can be damaged by particle fractures or interfacial decohesion, triggering ductile fractures in aluminium. Coarse intermetallic particles may be formed during heat treatment processes due to heterogeneous nucleation or overageing, but they are also often formed during casting, and they remain until after thermo-mechanical treatments. In such cases, as shown in Fig. 8, they are not only coarse but also complex and distorted in shape. With regard to the in-situ strength of brittle particles, such as intermetallic compounds, the size dependency of the in-situ strength is understood to be based on the weakest link theory [46], and the effects of particle shape are mainly on local stress concentrations. In this study, statistical analysis was applied to cases where the fractures of brittle particles in the order of 10,000 particles of various shapes and sizes was mainly governed by the weakest link theory and local stress concentrations and where particle damage was partially accelerated by hydrogen. In general, direct visualisation of hydrogen, the smallest element, is difficult, but it is possible to estimate its location in aluminium. For this purpose, it was necessary to identify all hydrogen trap sites in the aluminium alloys, determine their spatial distribution, and know the capacity of the hydrogen trap sites (i.e., the density of the hydrogen trap sites and the hydrogen binding energy).

The main hydrogen trap sites in Al—Zn—Mg alloys are solute Mg atoms (hydrogen trap energy of 11.6 kJ/mol), grain boundaries (19.3 kJ/mol), screw dislocations (10.6 kJ/mol), edge dislocations (17.4 kJ/mol), vacancies (28.9 kJ/mol), the inner surface of pores (67.5 kJ/mol), coherent interfaces between $MgZn_2$ precipitates and aluminium (7.9–33.9 kJ/mol), and semi-coherent interfaces between $MgZn_2$ precipitates and aluminium (53.8 kJ/mol) [32]. Su et al. prepared aluminium alloys with a considerably high Zn content of 10 mass%, and measured the 3D spatial distribution and density of the above-mentioned hydrogen trap sites using high-resolution X-ray CT [27]. The results showed that the hydrogen trap energy of the pores was the highest, but their trap site density was relatively low due to the two-dimensional hydrogen trap sites on the inner surface of the coarse pores. Therefore, the hydrogen trap sites of the pores were saturated with hydrogen in high hydrogen concentration materials with a hydrogen concentration of 6.97 mass ppm [27]. As a result, most of the hydrogen in the materials was concentrated at the $MgZn_2$ precipitate/aluminium interface [23].

Tsuru et al. performed first-principles simulations for $MgZn_2$ precipitate/aluminium interfaces with high hydrogen concentrations [26]. They found that as the hydrogen concentration at the $MgZn_2$ precipitate/aluminium interfaces increases, the interfacial cohesive energy decreases linearly and drops to almost zero above hydrogen concentrations of 20 atom/nm^2 [26]. This is a phenomenon specific to aluminium and is attributed to its low surface energy. Interestingly, their simulations reproduced the spontaneous decohesion of the $MgZn_2$ precipitate/aluminium interface in the absence of external loading [26].

Based on the understanding of such hydrogen embrittlement mechanisms in Al—Zn—Mg alloys, Fujihara et al. [47] and Wang et al. [32] reported hydrogen partitioning at each hydrogen trap site and hydrogen embrittlement behaviour of aluminium alloys when specific intermetallic compounds other than $MgZn_2$ were added to Al—Zn—Mg alloys. In this case, the Al_7Cu_2Fe particles with hydrogen trap sites with high hydrogen trap energy inside the particles (54.0 kJ/mol) were added together with Mg_2Si particles with hydrogen trap energy inside the particles close to zero (−29.9 ∼ −19.3 kJ/mol [33]) but with particle/aluminium interfaces with high hydrogen trap energy (33.8 ∼ 77.2 kJ/mol [48]) [32]. As a result, most of the hydrogen was trapped at the $MgZn_2$ precipitate/aluminium interface in the absence of Al_7Cu_2Fe particles, whereas when Al_7Cu_2Fe particles were added, they stored the most hydrogen of all the trapping sites. In exchange, the hydrogen concentration at the $MgZn_2$ precipitate/aluminium interface was significantly reduced. It has been experimentally confirmed [32] that this effectively suppresses hydrogen embrittlement of aluminium alloys.

This study shows that hydrogen does not directly contribute to the damage of Al_7Cu_2Fe particles. The fracture of Al_7Cu_2Fe at high hydrogen concentrations has not been studied by a physical simulation, as in the case of the above-mentioned spontaneous debonding of the $MgZn_2$ precipitate/aluminium interface. However, the results of the present study suggest that even the crystallographic planes of Al_7Cu_2Fe with the lowest hydrogen trapping energy have a sufficiently large cohesive energy and that even if hydrogen is trapped to some extent, the reduction in cohesive energy is limited and the particles themselves have sufficient residual strength. This is also because Al_7Cu_2Fe particles have three-dimensional hydrogen trap sites inside them, which is extremely advantageous in terms of trap site density compared to the two-dimensional nature of the interfacial trap sites of $MgZn_2$ precipitates and Mg_2Si particles. In fact, according to the analysis of Wang et al., although Al_7Cu_2Fe particles are the hydrogen trap sites that absorb the most hydrogen in aluminium alloys, the amount of hydrogen in an internal hydrogen trap site does not even reach 1/100 [32]. The LH material had a hydrogen concentration of 3.1 mass ppm, which is more than one order of magnitude higher than that of practical alloys (typically 0.2 mass ppm or less). This means that practical alloys have even more hydrogen storage capacity than the LH material. This indicates the effectiveness of using particles with three-dimensional hydrogen trapping sites in their interiors to prevent hydrogen embrittlement of aluminium alloys. Unfortunately, to date, the fracture behaviour inside Al_7Cu_2Fe particles and the hydrogen trapping and interfacial cohesive energy of the Al_7Cu_2Fe particle/aluminium interface have not been computationally investigated. So, at very high hydrogen concentrations of tens or hundreds of massppm, which would be impractical for practical materials, we can only wait for further experimental investigations to determine at which hydrogen levels the damage of Al_7Cu_2Fe particles is conducive and if the interface debonding occurs preferentially in such a case.

It should be noted, however, that the deformation behaviour of the aluminium matrix is more or less affected by hydrogen, as shown in Fig. 7. Interestingly, Wang et al. have shown that the hydrogen concentration at the $MgZn_2$ precipitate/aluminium interface can vary locally by more than three orders of magnitude due to heterogeneously dispersed Al_7Cu_2Fe particles [32]. Therefore, when preventing hydrogen embrittlement of aluminium alloys by dispersion of Al_7Cu_2Fe particles, the key issue is to ensure that Al_7Cu_2Fe particles are dispersed as uniformly and finely as possible.

On the other hand, the occupancy of a hydrogen trap site at the Mg_2Si particle/aluminium interface reaches close to 1 [32]. And it has been experimentally confirmed [32] that the hydrogen promotes the decohesion of the Mg_2Si particle/aluminium interface. Although this has not been proven by physical simulations, unlike the case of spontaneous decohesion of the $MgZn_2$ precipitate/aluminium interface [33], it suggests that particle damage may also occur at high hydrogen

concentrations in the case of the Mg_2Si particle/aluminium interface. It can be inferred that the interfacial cohesive energy at the Mg_2Si particle interface is much lower than the inside of Al_7Cu_2Fe particle and that hydrogen enrichment significantly reduces this, resulting in debonding at a lower interfacial stress than in the absence of hydrogen. The reduction in ductility of aluminium alloys at high hydrogen concentrations, as observed in Fig. S1, may be partly due to such a mechanism. In other words, even if the macroscopic fracture mode of aluminium is ductile fracture, hydrogen may cause a reduction in macroscopic properties, such as ductility, and this can be regarded as a form of hydrogen embrittlement of aluminium. Hydrogen embrittlement of the aluminium itself and the enhancement of ductile fracture by particle fracture or interfacial debonding are assumed to be competitively selected. This will depend on various conditions such as material microstructure and hydrogen concentration. It is not straightforward, because even if particle damage is locally promoted, this does not necessarily affect the overall fracture. This phenomenon, when directly linked to hydrogen embrittlement, has been referred to in the literature as local HEDE micro-incidents and has already been discussed in the context of various other materials [49].

5.2. Microstructural control considering particle damage and fracture surface formation

As shown in Fig. 8(b), the surrogate model that represents the damage behaviour of all the visible particles (objective function I_1) and the model that only evaluates the tendency of fracture surface formation for damaged particles (objective function I_2) are diametrically opposed in terms of optimal particle size. Specifically, the particles optimising objective function I_1 were small in diameter but were relatively large for function I_2. This may be because coarse particles tend to exist independently, but particle clusters are composed of relatively small particles. In this study, most of the design variables representing the spatial distribution of particles were eliminated in the design variable coarsening processes. However, the principal component analysis used in this study had difficulty in detecting relatively weak interdependencies, such as size and spatial distribution and shape and spatial distribution. In order to understand the physical implications of the surrogate model, it is useful to add analysis using copulas, etc. so that specific variables are not central to the interaction, and they can also reflect complex dependency structures, hem-dependencies, etc.

It should be noted that macroscopic fractures based on particle damage involve a series of processes, where the particle properties lead to particle damage, and then the damaged particles lead to the final fracture. So damage and fracture surface formation are not separated as they are in the analyses in this study (i.e., the objective functions I_1 and I_2 were separated). In general, the main cracks that cause macroscopic fractures in a material are often limited to a single or small number of cracks. Their formation is often caused by strain localisation due to hydrogen, stress concentrations on surface scratches, and local material microstructural heterogeneities, such as PFZ and coarse grains. These factors were not incorporated into the design variables used in this study. Therefore, if a new objective function combining the objective functions I_1 and I_2 is set up and an attempt is made to evaluate the fracture surface formation tendency of the material for all the visible particles, these factors would significantly impair the accuracy of the statistical analysis. Therefore, in this study, statistical analysis was carried out separately for the surrogate model that evaluated the damage behaviour for all the particles from the model that evaluated the fracture surface formation tendency for only the damaged particles. From a practical point of view, in order to identify a microstructural morphology that can reduce the macroscopic degradation in mechanical properties due to particle damage, it is reasonable to evaluate the damage behaviour for all the particles using the objective function I_1. If this evaluation is to be developed further, a more refined evaluation of the relationship between particle properties and particle clustering is required.

6. Conclusion

Methods to prevent hydrogen embrittlement of aluminium alloys by dispersing intermetallic compound particles with a strong capacity to trap hydrogen have been proposed in previous research. However, there has been a concern that the intermetallic compound particles themselves, which absorb large amounts of hydrogen, may be damaged due to hydrogen embrittlement.

In this study, 4D observations of hydrogen embrittlement in aluminium were carried out to obtain data on the damage behaviour of a large number of particles dispersed in a single tensile specimen. The Al_7Cu_2Fe and Mg_2Si particles dispersed in the A7075 alloy specimen had hydrogen trap sites with high hydrogen trap energy inside the particles and at the particle/aluminium interface. Two objective functions were set up to assess the ease of particle damage and fracture surface formation of damaged particles to elucidate the effects of the properties of the particles and of hydrogen. Another purpose was to identify and demonstrate the strongest and weakest particles. To identify the damaged particles that constituted fracture surfaces, 4D image analysis for fracture path identification was applied to unloaded and in-progress 3D images. The statistical analysis method integrated thorough particle characterisation using a number of design variables, two coarsening processes, and surrogate modelling. For surrogate modelling, support vector machines were combined with the infill sampling criteria to perform statistical analysis suitable for relatively small data sets ranging in size from 372 to 13,229 particles.

A total of 43 design variables were prepared and then reduced to between four and seven by taking into account data independence and correlation with the objective functions. In the coarsening processes, many design variables representing particle size and shape remained, while those relating to the spatial distribution of particles tended to be eliminated.

As a result, surrogate models could be constructed that reflected stochastic particle damage behaviour and were adequate to perform evaluations. No change in particle damage behaviour or the tendency to form fracture surfaces was observed with increasing hydrogen concentrations. This suggests that Al_7Cu_2Fe particles do not exhibit hydrogen embrittlement. It is therefore concluded that the dispersion of Al_7Cu_2Fe particles is effective in preventing hydrogen embrittlement of aluminium. It was also found during tensile loading that only particles that were very coarse and had very complex shapes were damaged. In terms of particle shapes, shape discontinuities, elongation, and orientation in the loading direction that led to stress concentration and increased stress triaxiality were found to be of crucial importance. On the other hand, for Mg_2Si particles, the influence of hydrogen was shown to advocate particle damage. In addition, actual damaged particles with design variable values closest to the weakest and strongest particles predicted by the surrogate model were extracted from the experimental data for visual evaluation. Interestingly, particles with a high propensity to form fracture surfaces were predicted to be small and relatively simple in shape for both Al_7Cu_2Fe and Mg_2Si particles. This was considered to be because particle clusters are composed of relatively small particles, but coarse particles tend to exist independently. Finally, the guiding principles for preventing hydrogen embrittlement of aluminium are discussed in terms of the link between the hydrogen embrittlement of particles and that of aluminium.

CRediT authorship contribution statement

Hiroyuki Toda: Writing – original draft, Supervision, Funding acquisition, Conceptualization. **Yuki Fukuda:** Validation, Investigation, Formal analysis, Data curation, Conceptualization. **Han Li:** Software, Methodology. **Kyosuke Hirayama:** Writing – review & editing, Investigation, Formal analysis. **Hiro Fujihara:** Writing – review & editing,

Visualization, Investigation, Formal analysis, Data curation. **Kazuyuki Shimizu:** Writing – review & editing, Investigation, Formal analysis. **Yafei Wang:** Writing – review & editing, Investigation, Formal analysis. **Jianwei Tang:** Writing – review & editing, Investigation, Formal analysis. **Akihisa Takeuchi:** Software, Methodology. **Masayuki Uesugi:** Software, Methodology.

Declaration of competing interest

The authors declare that they have no known competing financial interests or personal relationships that could have appeared to influence the work reported in this paper.

Acknowledgments

This research was funded by the JST Strategic Basic Research Program (CREST) "Elucidation of macroscale mechanical properties based on understanding nanoscale dynamics for innovative mechanical materials" (Grant number JPMJCR1995). In addition, part of this research was supported by the Light Metal Educational Foundation. Furthermore, synchrotron radiation experiments were carried out under SPring-8 projects (2019B2046, 2020A1084, 2020A1796, 2021A1002, 2021B1123, 2022A1005). These are noted and deeply appreciated.

Supplementary materials

Supplementary material associated with this article can be found, in the online version, at doi:10.1016/j.actamat.2024.120391.

References

[1] R.G. Song, W. Dietzel, B.J. Zhang, W.J. Liu, M.K. Tseng, A. Atrens, Stress corrosion cracking and hydrogen embrittlement of an Al–Zn–Mg–Cu alloy, Acta Mater. 52 (2004) 4727–4743, https://doi.org/10.1016/j.actamat.2004.06.023.
[2] A. Turnbull, J.R. Scully, A model for hydrogen enhanced decohesion of grain boundaries, Acta Mater. 49 (2001) 845–855.
[3] H.K. Birnbaum, S.R. Sofronis, Hydrogen-enhanced localized plasticity - a mechanism for hydrogen-related fracture, Mater. Sci. Eng. A 176 (1994) 191–202.
[4] J.R. Scully, D.J. Robertson, Hydrogen-enhanced localized plasticity in aluminium alloys, Int. Mater. Rev. 55 (2010) 105–123.
[5] N. Nagao, T. Muto, T. Nishimura, Atomic scale understanding of hydrogen enhanced vacancy formation in nickel, Acta Mater 59 (2011) 1108–1117.
[6] M.B. Djukic, G.M. Bakic, V.S. Zeravcic, A. Sedmak, B. Rajicic, The synergistic action and interplay of hydrogen embrittlement mechanisms in steels and iron: localized plasticity and decohesion, Eng. Fract. Mech. 216 (2019) 106528.
[7] N.J.H. Holroyd, D. Hardie, Strain-rate effects in the environmentally assisted fracture of a commercial high-strength aluminium alloy (7049), Corros. Sci. 21 (1981) 129–144, https://doi.org/10.1016/0010-938X(81)90097-4.
[8] B.K. M, V.S. Raja, Hydrogen embrittlement susceptibility of over aged 7010 Al-alloy, J. Mater. Sci. 41 (2006) 5495–5499, https://doi.org/10.1007/s10853-006-0287-1.
[9] G.A. Young, J.R. Scully, The effects of test temperature, temper, and alloyed copper on the hydrogen-controlled crack growth rate of an Al-Zn-Mg-(Cu) alloy, Metall. Mater. Trans. A 33 (2002) 1167–1181, https://doi.org/10.1007/s11661-002-0218-y.
[10] A. Thakur, R. Raman, S.N. Malhotra, Hydrogen embrittlement studies of aged and retrogressed-reaged Al-Zn-Mg alloys, Mater. Chem. Phys. 101 (2007) 441–447, https://doi.org/10.1016/j.matchemphys.2006.08.004.
[11] S. Osaki, D. Itoh, M. Nakai, SCC properties of 7050 series aluminum alloys in T6 and RRA tempers, J. Japan Inst. Light Met. 51 (2001) 222–227, https://doi.org/10.2464/jilm.51.222.
[12] G. Peng, K. Chen, S. Chen, H. Fang, Influence of repetitious-RRA treatment on the strength and SCC resistance of Al-Zn-Mg-Cu alloy, Mater. Sci. Eng. A 528 (2011) 4014–4018, https://doi.org/10.1016/j.msea.2011.01.088.
[13] G. Itoh, K. Hiyama, B.F. Lyu, J. Kobayashi, Suppression of intergranular fracture in 7000 series aluminum alloys, Mater. Sci. Forum. 1016 (2021) 1811–1815, https://doi.org/10.4028/www.scientific.net/MSF.1016.1811.
[14] Y.L. Wu, F.H. Froes, C. Li, A. Alvarez, Microalloying of Sc, Ni, and Ce in an advanced Al-Zn-Mg-Cu alloy, Metall. Mater. Trans. A Phys. Metall. Mater. Sci. 30 (1999) 1017–1024, https://doi.org/10.1007/s11661-999-0154-1.
[15] T. Hiramatsu, M. Chikuda, Y. Miyagi, M. Hirano, Effects of small amounts of additional elements on directionality of stress corrosion resistance of the Al-Zn-Mg alloys, J. Japan Inst. Light Met. 23 (1973) 210–217, https://doi.org/10.2464/jilm.23.210.
[16] M.K.B. Day, A.J. Cornish, T.P. Dent, The relationship between structure and stress-corrosion life in an Al–Zn–Mg alloy, Met. Sci. J. 3 (1969) 175–182, https://doi.org/10.1179/msc.1969.3.1.175.
[17] Y. Deng, Z. Yin, K. Zhao, J. Duan, Z. He, Effects of Sc and Zr microalloying additions on the microstructure and mechanical properties of new Al-Zn-Mg alloys, J. Alloys Compd. 530 (2012) 71–80, https://doi.org/10.1016/j.jallcom.2012.03.108.
[18] S. Chen, K. Chen, P. Dong, S. Ye, L. Huang, Effect of recrystallization and heat treatment on strength and SCC of an Al-Zn-Mg-Cu alloy, J. Alloys Compd. 581 (2013) 705–709, https://doi.org/10.1016/j.jallcom.2013.07.177.
[19] M.B. Kannan, V.S. Raja, A.K. Mukhopadhyay, P. Schmuki, Environmentally assisted cracking behavior of peak-aged 7010 aluminum alloy containing scandium, Metall. Mater. Trans. A. 36 (2005) 3257–3262, https://doi.org/10.1007/s11661-005-0098-z.
[20] Y. Shi, Q. Pan, M. Li, X. Huang, B. Li, Effect of Sc and Zr additions on corrosion behaviour of Al-Zn-Mg-Cu alloys, J. Alloys Compd. 612 (2014) 42–50, https://doi.org/10.1016/j.jallcom.2014.05.128.
[21] H.C. Fang, H. Chao, K.H. Chen, Effect of recrystallization on intergranular fracture and corrosion of Al-Zn-Mg-Cu-Zr alloy, J. Alloys Compd. 622 (2015) 166–173, https://doi.org/10.1016/j.jallcom.2014.10.044.
[22] K.H. Chen, H.C. Fang, Z. Zhang, X. Chen, G. Liu, Effect of of Yb, Cr and Zr additions on recrystallization and corrosion resistance of Al-Zn-Mg-Cu alloys, Mater. Sci. Eng. A 497 (2008) 426–431, https://doi.org/10.1016/j.msea.2008.07.028.
[23] M. Yu, Y. Zhang, X. Li, K. Wen, B. Xiong, Z. Li, L. Yan, H. Yan, H. Liu, Y. Li, Effect of recrystallization on plasticity, fracture toughness and stress corrosion cracking of a high-alloying Al-Zn-Mg-Cu alloy, Mater. Lett. 275 (2020) 128074, https://doi.org/10.1016/j.matlet.2020.128074.
[24] M. Wang, L. Huang, K. Chen, W. Liu, Influence of minor combined addition of Cr and Pr on microstructure, mechanical properties and corrosion behaviors of an ultrahigh strength Al-Zn-Mg-Cu-Zr alloy, Micron 104 (2018) 80–88, https://doi.org/10.1016/j.micron.2017.10.008.
[25] G. Li, N. Zhao, T. Liu, J. Li, C. He, C. Shi, E. Liu, J. Sha, Effect of Sc/Zr ratio on the microstructure and mechanical properties of new type of Al-Zn-Mg-Sc-Zr alloys, Mater. Sci. Eng. A 617 (2014) 219–227, https://doi.org/10.1016/j.msea.2014.08.041.
[26] T. Tsuru, K. Shimizu, M. Yamaguchi, M. Itakura, K. Ebihara, A. Bendo, K. Matsuda, H. Toda, Hydrogen-accelerated spontaneous microcracking in high-strength aluminium alloys, Sci. Rep. 10 (2020) 1998, https://doi.org/10.1038/s41598-020-58834-6.
[27] H. Su, H. Toda, K. Shimizu, K. Uesugi, A. Takeuchi, Y. Watanabe, Assessment of hydrogen embrittlement via image-based techniques in Al–Zn–Mg–Cu aluminum alloys, Acta Mater. 176 (2019) 96–108, https://doi.org/10.1016/j.actamat.2019.06.056.
[28] R. Oikawa, K. Shimizu, Y. Kamada, H. Toda, H. Fujihara, M. Uesugi, A. Takeuchi, Influence of hydrogen on the damage behavior of IMC particles in Al-Zn-Mg-Cu alloys, J. Jpn. Inst. Light Met. 72 (2022) 720702, https://doi.org/10.2464/jilm.72.411.
[29] Y. Xu, H. Toda, K. Shimizu, Y. Wang, B. Gault, W. Li, K. Hirayama, H. Fujihara, X. Jin, A. Takeuchi, M. Uesugi, Suppressed hydrogen embrittlement of high-strength Al alloys by Mn-rich intermetallic compound particles, Acta Mater. 236 (2022) 118110, https://doi.org/10.1016/j.actamat.2022.118110.
[30] Y. Wang, B. Sharma, Y. Xu, K. Shimizu, H. Fujihara, K. Hirayama, A. Takeuchi, M. Uesugi, G. Cheng, H. Toda, Switching nanoprecipitates to resist hydrogen embrittlement in high-strength aluminum alloys, Nat. Commun. 13 (2022) 6860, https://doi.org/10.1038/s41467-022-34628-4.
[31] H. Toda, M. Yamaguchi, T. Tsuru, K. Shimizu, K. Matsuda, K. Hirayama, Tomography for bridging nano and macro: semi-spontaneous iinterfacial debonding, Mater. Jpn. 60 (2021) 13–18, https://doi.org/10.2320/materia.60.13.
[32] Y. Wang, H. Toda, Y. Xu, K. Shimizu, K. Hirayama, H. Fujihara, A. Takeuchi, M. Uesugi, In-situ 3D observation of hydrogen-assisted particle damage behavior in 7075 Al alloy by synchrotron X-ray tomography, Acta Mater. 227 (2022) 117658, https://doi.org/10.1016/j.actamat.2022.117658.
[33] M. Yamaguchi, T. Tsuru, K. Ebihara, M. Itakura, K. Matsuda, K. Shimizu, H. Toda, Hydrogen trapping in Mg2Si and Al7FeCu2 intermetallic compounds in aluminum alloy: first-principles calculations, Mater. Trans. 61 (2020) 1907–1911, https://doi.org/10.2320/matertrans.MT-M2020201.
[34] H. Toda, H. Oogo, K. Uesugi, M. Kobayashi, Roles of pre-existing hydrogen micropores on ductile fracture, Mater. Trans. 50 (2009) 2285–2290, https://doi.org/10.2320/matertrans.M2009123.
[35] H. Toda, H. Oogo, K. Horikawa, K. Uesugi, A. Takeuchi, Y. Suzuki, M. Nakazawa, Y. Aoki, M. Kobayashi, The true origin of ductile fracture in aluminum alloys, Metall. Mater. Trans. A Phys. Metall. Mater. Sci. 45 (2014) 765–776, https://doi.org/10.1007/s11661-013-2013-3.
[36] I.M. Robertson, P. Sofronis, A. Nagao, M.L. Martin, S. Wang, D.W. Gross, K. E. Nygren, Hydrogen embrittlement understood, Metall. Mater. Trans. A 46 (2015) 2323–2341, https://doi.org/10.1007/s11661-015-2836-1.
[37] H. Toda, H. Li, R. Batres, K. Hirayama, H. Fujihara, Surrogate-based optimization of microstructural features of structural materials, Acta Mater. 257 (2023) 119188, https://doi.org/10.1016/j.actamat.2023.119188.
[38] H. Toda, K. Hirayama, H. Li, R. Batres, D. Seo, H. Fujihara, Maximising mechanical properties of aluminium alloys by microstructural optimisation using a coarsened surrogate model, Comput. Mater. Sci. 243 (2024) 113115.
[39] H. Toda, K. Hirayama, S. Yamaguchi, H. Fujihara, R. Higa, K. Shimizu, A. Takeuchi, M. Uesugi, Dominant factors controlling the initiation of hydrogen embrittlement in Al–Zn–Mg Alloy, Mater. Trans. 64 (2023) 2729–2738, https://doi.org/10.2320/matertrans.MT-M2023116.
[40] H. Su, H. Toda, R. Masunaga, K. Shimizu, H. Gao, K. Sasaki, M.S. Bhuiyan, K. Uesugi, A. Takeuchi, Y. Watanabe, Influence of hydrogen on strain localization

and fracture behavior in Al Zn Mg Cu aluminum alloys, Acta Mater. 159 (2018) 332–343, https://doi.org/10.1016/j.actamat.2018.08.024.
[41] M.S. Bhuiyan, Y. Tada, H. Toda, S. Hang, K. Uesugi, A. Takeuchi, N. Sakaguchi, Y. Watanabe, Influences of hydrogen on deformation and fracture behaviors of high Zn 7XXX aluminum alloys, Int. J. Fract. 200 (2016) 13–29, https://doi.org/10.1007/s10704-016-0092-z.
[42] H. Toda, K. Minami, K. Koyama, K. Ichitani, M. Kobayashi, K. Uesugi, Y. Suzuki, Healing behavior of preexisting hydrogen micropores in aluminum alloys during plastic deformation, Acta Mater. 57 (2009) 4391–4403, https://doi.org/10.1016/j.actamat.2009.06.012.
[43] H. Toda, C.T. X-Ray, Hardware and Software Techniques, Springer Nature, Singapore, 2021.
[44] M. Kobayashi, H. Toda, Y. Kawai, T. Ohgaki, K. Uesugi, D.S. Wilkinson, T. Kobayashi, Y. Aoki, M. Nakazawa, High-density three-dimensional mapping of internal strain by tracking microstructural features, Acta Mater. 56 (2008) 2167–2181, https://doi.org/10.1016/j.actamat.2007.12.058.
[45] P.J. Withers, W.M. Stobbs, O.B. Pedersen, The application of the eshelby method of internal stress determination to short fibre metal matrix composites, Acta Metall. 37 (1989) 3061–3084, https://doi.org/10.1016/0001-6160(89)90341-6.
[46] W. Weibull, A statistical distribution function of wide applicability, J. Appl. Mech. 18 (1951) 293–297, https://doi.org/10.1115/1.4010337.
[47] H. Fujihara, K. Shimizu, H. Toda, A. Takeuchi, M. Uesugi, Suppression of hydrogen embrittlement due to local partitioning of hydrogen to dispersed intermetallic compound particles in Al–Zn–Mg–Cu alloys, Mater. Trans. 63 (2022) 1406–1415, https://doi.org/10.2320/matertrans.MT-L2022007.
[48] M. Yamaguchi, K.I. Ebihara, T. Tsuru, M. Itakura, First-principles calculations of hydrogen trapping energy on incoherent interfaces of aluminum alloys, Mater. Trans. 64 (2023) 2553–2559, https://doi.org/10.2320/matertrans.MT-M2023106.
[49] M. Wasim, M. Djukic, T.D. Ngo, Influence of hydrogen-enhanced plasticity and decohesion mechanisms of hydrogen embrittlement on the fracture resistance of steel, Eng. Failure Anal. 123 (2021) 105312.